PERGAMON

Engineering Fracture Mechanics 70 (2003) 1–27

Engineering Fracture Mechanics

www.elsevier.com/locate/engfracmech

Mesh-free analysis of cracks in isotropic functionally graded materials

B.N. Rao, S. Rahman *

College of Engineering, The University of Iowa, 2140 Seamans Center, Iowa City, IA 52242, USA

Received 21 August 2001; received in revised form 22 February 2002; accepted 17 March 2002

Abstract

This paper presents a Galerkin-based meshless method for calculating stress-intensity factors (SIFs) for a stationary crack in two-dimensional functionally graded materials of arbitrary geometry. The method involves an element-free Galerkin method (EFGM), where the material properties are smooth functions of spatial coordinates and two newly developed interaction integrals for mixed-mode fracture analysis. These integrals can also be implemented in conjunction with other numerical methods, such as the finite element method (FEM). Five numerical examples including both mode-I and mixed-mode problems are presented to evaluate the accuracy of SIFs calculated by the proposed EFGM. Comparisons have been made between the SIFs predicted by EFGM and available reference solutions in the literature, generated either analytically or by FEM using various other fracture integrals or analyses. A good agreement is obtained between the results of the proposed meshless method and the reference solutions.

Keywords: Crack; Functionally graded materials; Element-free Galerkin method; Stress-intensity factor; *J*-integral; Interaction integral

1. Introduction

In recent years, functionally graded materials (FGMs) have been introduced and applied in the development of structural components subject to non-uniform service requirements. FGMs, which possess continuously varying microstructure and mechanical and/or thermal properties, are essentially two-phase particulate composites, such as ceramic and metal alloy phases, synthesized such that the composition of each constituent changes continuously in one direction, to yield a predetermined composition profile [1]. Even though the initial developmental emphasis of FGMs was to synthesize thermal barrier coating for space applications [2], later investigations uncovered a wide variety of potential applications, including nuclear fast breeder reactors [3], piezoelectric and thermoelectric devices [4–6], graded refractive index

* Corresponding author. Tel.: +1-319-335-5679; fax: +1-319-335-5669.
E-mail address: rahman@engineering.uiowa.edu (S. Rahman).
URL: http://www.engineering.uiowa.edu/~rahman.

0013-7944/03/$ - see front matter © 2002 Elsevier Science Ltd. All rights reserved.
PII: S0013-7944(02)00038-3

materials in audio–video disks [7], thermionic converters [8], dental and medical implants [9], and others [10]. The absence of sharp interfaces in FGM largely reduces material property mismatch, which has been found to improve resistance to interfacial delamination and fatigue crack propagation [11]. However, the microstructure of FGM is generally heterogeneous, and the dominant type of failure in FGM is crack initiation and growth from inclusions. The extent to which constituent material properties and microstructure can be tailored to guard against potential fracture and failure patterns is relatively unknown. Such issues have motivated much of the current research into the numerical computation of crack-driving forces and the simulation of crack growth in FGMs.

Analytical work on FGMs begins as early as 1960 when soil was modeled as a non-homogeneous material by Gibson [12]. Due to the complexity, plane elasticity problems involving cracks in FGM are solved assuming a functional form of the material property variation, usually a linear or exponential function. Assuming an exponential spatial variation of the elastic modulus, Atkinson and List [13], Dhaliwal and Singh [14], and Delale and Erdogan [15] solved crack problems for non-homogeneous materials subjected to mechanical loads. Delale and Erdogan [15] showed that the asymptotic crack-tip stress field in FGMs possesses the same square root singularity as in homogeneous materials. Eischen [16] studied mixed-mode conditions in non-homogeneous materials using the finite element method (FEM). He also verified that the leading term of the asymptotic expansion for stresses was square-root singular. This result was reconfirmed by Jin and Noda [17] for materials with piecewise differentiable property variations. By further assuming the exponential variation of thermal properties of the material, Jin and Noda [18] and Erdogan and Wu [19] computed thermal stress-intensity factor (SIF) for non-homogeneous solids. Yang and Shih [20] considered a semi-infinite crack in an interlayer between two dissimilar materials, and they obtained an approximate solution from a known bimaterial solution. Gu and Asaro [21] considered a semi-infinite crack in a strip of FGM under edge loading and obtained SIF relations for many commonly used fracture specimen configurations. Erdogan [11] reviewed the elementary concepts of fracture mechanics of FGM and identified a number of typical problems relating to FGM fracture. Crack deflection in FGM has been considered by Gu and Asaro [22] who reported the strong influence of the material gradient on the crack kink angle when the crack is in the middle of the gradient zone. Tohgo et al. [23] carried out a numerical analysis of particulate FGM, and studied the influence of the material gradient on the size of a singular field by comparing the FGM results with those obtained for a homogeneous medium. Gu et al. [24] presented a simplified method for calculating the crack-tip field of FGMs using the equivalent domain integral technique. Anlas et al. [25] evaluated SIFs in FGMs by the FEM where the material property variation was discretized by assigning different homogeneous elastic properties to each element. Both Gu et al. [24] and Anlas et al. [25] considered a mode-I crack where the crack is parallel to the material gradation, and used commercial FEM software in their analyses. Marur and Tippur [26] considered a crack normal to the elastic gradient and performed FEM analysis in conjunction with their experiments. Bao and Wang [27] studied multi-cracking in an FGM coating. Bao and Cai [28] studied delamination cracking in a functionally graded ceramic/metal substrate. Lee and Erdogan [29] evaluated residual thermal stresses in FGMs. Recently, Kim and Paulino [30] evaluated the mixed-mode fracture parameters in FGMs using FEM analysis with three different approaches: the path-independent J_k^*-integral method, the modified crack-closure integral method, and the displacement correlation technique. Zou et al. [31] proposed a multiple isoparametric FEM to evaluate the SIFs of cracks in FGMs. Thus, most of the analytical studies on FGM reviewed above have used FEM as the numerical tool. FEM may present some limitations in solving solid mechanics problems characterized by a continuous change in geometry of the domain under analysis. Crack propagation is a prime example in which the use of FEM requires a large number of remeshings of the finite element model to represent arbitrary and complex paths. The underlying structures of FEM and similar methods, which rely on a mesh, is quite cumbersome in treating cracks that are not coincident with the original mesh geometry. Consequently, the only viable option for dealing with moving cracks using FEM is to remesh during each discrete step of model evolution so that the mesh lines remain coincident with the cracks throughout the

analysis. This creates numerical difficulties, often leading to degradation of solution accuracy, complexity in computer programming, and a computationally intensive environment.

In recent years, various Galerkin-based meshless or mesh-free methods have been developed or investigated to solve fracture-mechanics problems without the use of a structured grid [32–38]. These meshless methods employ moving least-squares (MLS) approximation of a function that permits the resultant shape functions to be constructed entirely in terms of arbitrarily placed nodes. Since no element connectivity data is required, the burdensome meshing or remeshing characteristic of FEM is avoided. Since the mesh generation of complex cracked structures can be a far more time-consuming and costly effort than the solution of a discrete set of linear equations, the meshless method provides an attractive alternative to FEM. However, to date most developments in meshless methods have focused on the fracture of homogeneous materials. Fracture analysis of cracks in FGMs using meshless methods has not been widespread and is only currently gaining attention. As a result, there is considerable interest in developing meshless methods for the evaluation of crack-driving force in FGMs.

This paper presents a meshless method for calculating the fracture parameters of a stationary crack in FGM with arbitrary geometry. This method involves an element-free Galerkin method (EFGM), where the material properties are smooth functions of spatial coordinates and two newly developed interaction integrals for mixed-mode fracture analysis. In conjunction with the proposed method, both mode-I and mixed-mode two-dimensional problems have been solved. Five numerical examples are presented to evaluate the accuracy of SIFs calculated by the proposed method. Comparisons have been made between the SIFs predicted by the proposed method and the existing results available in the current literature.

2. Crack-tip fields in FGM

Consider a two-dimensional structure with a rectilinear crack of length $2a$, subjected to external loads $S_1, S_2, \ldots, S_M$, as shown in Fig. 1. It is assumed that the material properties, such as the modulus of elasticity E and the Poisson's ratio v, vary according to

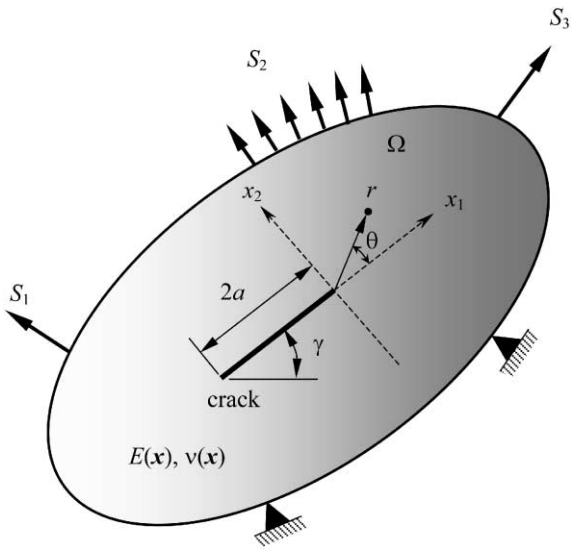

Fig. 1. A crack in a functionally graded material.

$$E = E(x_1, x_2) = E(\boldsymbol{x}), \tag{1}$$

$$v = v(x_1, x_2) = v(\boldsymbol{x}), \tag{2}$$

where $\boldsymbol{x} = \{x_1, x_2\}^{\mathrm{T}} \in \Re^2$, $E(\boldsymbol{x}) \geqslant 0$ and $-1 \leqslant v(\boldsymbol{x}) \leqslant 1/2$ are continuous, bounded, and at least piecewise differentiable functions on domain Ω, and the x_1–x_2 coordinate system is defined in Fig. 1. In reality, FGMs are multi-phase materials with generally, locally discontinuous material properties. Hence, $E(\boldsymbol{x})$ and $v(\boldsymbol{x})$ in Eqs. (1) and (2) should be viewed as smoothly varying "effective" material properties of FGMs. In this case, FGMs can be modeled as non-homogeneous materials, for which the elastic constitutive equation is

$$\varepsilon_{ij} = \frac{1 + v^*(\boldsymbol{x})}{E^*(\boldsymbol{x})}\sigma_{ij} + \frac{v^*(\boldsymbol{x})}{E^*(\boldsymbol{x})}\sigma_{kk}\delta_{ij}, \tag{3}$$

where ε_{ij} and σ_{ij} are the strain and stress components, respectively, and δ_{ij} is the Kronecker delta. In Eq. (3), $E^*(\boldsymbol{x})$ and $v^*(\boldsymbol{x})$ are given by $E(\boldsymbol{x})$ and $v(\boldsymbol{x})$ under plane stress condition and by $E(\boldsymbol{x})/[1 - v(\boldsymbol{x})^2]$ and $v(\boldsymbol{x})/[1 - v(\boldsymbol{x})]$ under plane strain condition, respectively. For non-homogeneous materials undergoing plane stress or plane strain linear-elastic deformation, in the absence of body forces the Airy stress function $F(x_1, x_2)$ satisfies [16]

$$\nabla^2\left(\frac{\nabla^2 F}{E^*(\boldsymbol{x})}\right) - \frac{\partial^2}{\partial x_2^2}\left(\frac{1 + v^*(\boldsymbol{x})}{E^*(\boldsymbol{x})}\right)\frac{\partial^2 F}{\partial x_1^2} - \frac{\partial^2}{\partial x_1^2}\left(\frac{1 + v^*(\boldsymbol{x})}{E^*(\boldsymbol{x})}\right)\frac{\partial^2 F}{\partial x_2^2} + 2\frac{\partial^2}{\partial x_1 \partial x_2}\left(\frac{1 + v^*(\boldsymbol{x})}{E^*(\boldsymbol{x})}\right)\frac{\partial^2 F}{\partial x_1 \partial x_2} = 0, \tag{4}$$

where $\nabla^2 = \partial^2/\partial x_1^2 + \partial^2/\partial x_2^2$ is the two-dimensional Laplacian operator. Eischen [16] and later Jin and Noda [17] showed that for piecewise differentiable material property variations, the elastic stress and displacement fields in FGM can be derived using the stress function in variable separable form, identical to the homogeneous case. Hence, the linear-elastic singular stress field near the crack tip can be obtained as [16]

$$\sigma_{11} = \frac{1}{\sqrt{2\pi r}}[K_{\mathrm{I}} f_{11}^{\mathrm{I}}(\theta) + K_{\mathrm{II}} f_{11}^{\mathrm{II}}(\theta)], \tag{5}$$

$$\sigma_{22} = \frac{1}{\sqrt{2\pi r}}[K_{\mathrm{I}} f_{22}^{\mathrm{I}}(\theta) + K_{\mathrm{II}} f_{22}^{\mathrm{II}}(\theta)], \tag{6}$$

$$\sigma_{12} = \frac{1}{\sqrt{2\pi r}}[K_{\mathrm{I}} f_{12}^{\mathrm{I}}(\theta) + K_{\mathrm{II}} f_{12}^{\mathrm{II}}(\theta)], \tag{7}$$

where K_{I} and K_{II} are the mode-I and mode-II SIFs, respectively, and $f_{ij}^{\mathrm{I}}(\theta)$ and $f_{ij}^{\mathrm{II}}(\theta)$ ($i, j = 1, 2$) are the standard angular functions for a crack in a homogeneous elastic medium. Similarly, the near tip displacement field $\boldsymbol{u} = \{u_1, u_2\}^{\mathrm{T}}$ can be obtained as [16]

$$u_1 = \frac{1}{\mu_{\mathrm{tip}}}\sqrt{\frac{r}{2\pi}}[K_{\mathrm{I}} g_1^{\mathrm{I}}(\theta) + K_{\mathrm{II}} g_1^{\mathrm{II}}(\theta)] \tag{8}$$

and

$$u_2 = \frac{1}{\mu_{\mathrm{tip}}}\sqrt{\frac{r}{2\pi}}[K_{\mathrm{I}} g_2^{\mathrm{I}}(\theta) + K_{\mathrm{II}} g_2^{\mathrm{II}}(\theta)], \tag{9}$$

where $\mu_{\mathrm{tip}} = E_{\mathrm{tip}}/[2(1 + v_{\mathrm{tip}})]$ is the shear modulus, E_{tip} is the elastic modulus, and v_{tip} is the Poisson's ratio, all evaluated at the crack tip, and $g_i^{\mathrm{I}}(\theta)$ and $g_i^{\mathrm{II}}(\theta)$, $i = 1, 2$ are standard angular functions for a crack in a homogeneous elastic medium [39]. Even though the material gradient does not influence the square-root singularity or the singular stress distribution, the material gradient does affect the SIFs. Hence, the fracture parameters are functions of the material gradients, external loading, and geometry.

3. The interaction integral method

The interaction integral method is an effective tool for calculating mixed-mode fracture parameters in homogeneous materials [40,41]. In this section the interaction integral method for homogeneous materials is first briefly summarized, then extended for cracks in FGM. In fact, the study of FGM would enhance the understanding of a fracture in a generic material, since upon shrinking the gradient layer in FGM is expected to behave like a sharp interface, and upon expansion, the fracture behavior would be analogous to that of a homogeneous material.

3.1. Homogeneous materials

The path independent J-integral for a homogeneous cracked body is given by [42]

$$J = \int_{\Gamma} \left(W\delta_{1j} - \sigma_{ij}\frac{\partial u_i}{\partial x_1} \right) n_j \, \mathrm{d}\Gamma, \tag{10}$$

where $W = \int \sigma_{ij}\,\mathrm{d}\varepsilon_{ij}$ is the strain energy density and n_j is the jth component of the outward unit vector normal to an arbitrary contour Γ enclosing the crack tip. For linear elastic material models it can shown that $W = \sigma_{ij}\varepsilon_{ij}/2 = \varepsilon_{ij}D_{ijkl}\varepsilon_{kl}/2$, where D_{ijkl} is a component of constitutive tensor. Applying the divergence theorem, the contour integral in Eq. (10) can be converted into an equivalent domain form, given by [43]

$$J = \int_A \left(\sigma_{ij}\frac{\partial u_i}{\partial x_1} - W\delta_{1j} \right) \frac{\partial q}{\partial x_j} \, \mathrm{d}A + \int_A \frac{\partial}{\partial x_j}\left(\sigma_{ij}\frac{\partial u_i}{\partial x_1} - W\delta_{1j} \right) q \, \mathrm{d}A, \tag{11}$$

where A is the area inside the contour and q is a weight function chosen such that it has a value of *unity* at the crack tip, *zero* along the boundary of the domain, and arbitrary elsewhere. By expanding the second integrand, Eq. (11) reduces to

$$J = \int_A \left(\sigma_{ij}\frac{\partial u_i}{\partial x_1} - W\delta_{1j} \right) \frac{\partial q}{\partial x_j} \, \mathrm{d}A + \int_A \left(\frac{\partial \sigma_{ij}}{\partial x_j}\frac{\partial u_i}{\partial x_1} + \sigma_{ij}\frac{\partial^2 u_i}{\partial x_j \partial x_1} - \sigma_{ij}\frac{\partial \varepsilon_{ij}}{\partial x_1} - \frac{1}{2}\varepsilon_{ij}\frac{\partial D_{ijkl}}{\partial x_1}\varepsilon_{kl} \right) q \, \mathrm{d}A. \tag{12}$$

Using equilibrium ($\partial\sigma_{ij}/\partial x_j = 0$) and compatibility ($\varepsilon_{ij} = \partial u_i/\partial x_j$) conditions and noting that $\partial D_{ijkl}/\partial x_1 = 0$ in homogeneous materials, the second integrand of Eq. (12) vanishes, yielding

$$J = \int_A \left(\sigma_{ij}\frac{\partial u_i}{\partial x_1} - W\delta_{1j} \right) \frac{\partial q}{\partial x_j} \, \mathrm{d}A, \tag{13}$$

which is the classical domain form of the J-integral in homogeneous materials.

Consider two independent equilibrium states of the cracked body. Let state 1 correspond to the *actual* state for the given boundary conditions, and let state 2 correspond to an *auxiliary* state, which can be either mode-I or mode-II near tip displacement and stress fields. Superposition of these two states leads to another equilibrium state (state S) for which the domain form of the J-integral is

$$J^{(S)} = \int_A \left[(\sigma_{ij}^{(1)} + \sigma_{ij}^{(2)}) \frac{\partial (u_i^{(1)} + u_i^{(2)})}{\partial x_1} - W^{(S)}\delta_{1j} \right] \frac{\partial q}{\partial x_j} \, \mathrm{d}A, \tag{14}$$

where superscript $i = 1, 2$, and S indicate fields and quantities associated with state i and

$$W^{(S)} = \tfrac{1}{2}(\sigma_{ij}^{(1)} + \sigma_{ij}^{(2)})(\varepsilon_{ij}^{(1)} + \varepsilon_{ij}^{(2)}). \tag{15}$$

By expanding Eq. (14),

$$J^{(S)} = J^{(1)} + J^{(2)} + M^{(1,2)}, \tag{16}$$

where

$$J^{(1)} = \int_A \left[\sigma_{ij}^{(1)} \frac{\partial u_i^{(1)}}{\partial x_1} - W^{(1)} \delta_{1j} \right] \frac{\partial q}{\partial x_j} \, \mathrm{d}A \tag{17}$$

and

$$J^{(2)} = \int_A \left[\sigma_{ij}^{(2)} \frac{\partial u_i^{(2)}}{\partial x_1} - W^{(2)} \delta_{1j} \right] \frac{\partial q}{\partial x_j} \, \mathrm{d}A \tag{18}$$

are the J-integrals for states 1 and 2, respectively, and

$$M^{(1,2)} = \int_A \left[\sigma_{ij}^{(1)} \frac{\partial u_i^{(2)}}{\partial x_1} + \sigma_{ij}^{(2)} \frac{\partial u_i^{(1)}}{\partial x_1} - W^{(1,2)} \delta_{1j} \right] \frac{\partial q}{\partial x_j} \, \mathrm{d}A \tag{19}$$

is an interaction integral. In Eqs. (17)–(19), $W^{(1)} = \frac{1}{2}\sigma_{ij}^{(1)}\varepsilon_{ij}^{(1)}$, $W^{(2)} = \frac{1}{2}\sigma_{ij}^{(2)}\varepsilon_{ij}^{(2)}$, and $W^{(1,2)} = \frac{1}{2}(\sigma_{ij}^{(1)}\varepsilon_{ij}^{(2)} + \sigma_{ij}^{(2)}\varepsilon_{ij}^{(1)})$ represent various strain energy densities, which satisfy

$$W^{(S)} = W^{(1)} + W^{(2)} + W^{(1,2)}. \tag{20}$$

For linear-elastic solids under mixed-mode loading conditions, the J-integral is also equal to the energy release rate and hence, the J-integral can be written as

$$J = \frac{1}{E^*}(K_{\mathrm{I}}^2 + K_{\mathrm{II}}^2). \tag{21}$$

Applying Eq. (21) to states 1, 2, and the superimposed state S gives

$$J^{(1)} = \frac{1}{E^*}(K_{\mathrm{I}}^{(1)^2} + K_{\mathrm{II}}^{(1)^2}), \tag{22}$$

$$J^{(2)} = \frac{1}{E^*}(K_{\mathrm{I}}^{(2)^2} + K_{\mathrm{II}}^{(2)^2}) \tag{23}$$

and

$$\begin{aligned} J^{(S)} &= \frac{1}{E^*}\left[(K_{\mathrm{I}}^{(1)} + K_{\mathrm{I}}^{(2)})^2 + (K_{\mathrm{II}}^{(1)} + K_{\mathrm{II}}^{(2)})^2\right] \\ &= \frac{1}{E^*}\left[(K_{\mathrm{I}}^{(1)^2} + K_{\mathrm{II}}^{(1)^2}) + (K_{\mathrm{I}}^{(2)^2} + K_{\mathrm{II}}^{(2)^2}) + 2(K_{\mathrm{I}}^{(1)}K_{\mathrm{I}}^{(2)} + K_{\mathrm{II}}^{(1)}K_{\mathrm{II}}^{(2)})\right] \\ &= J^{(1)} + J^{(2)} + \frac{2}{E^*}\left(K_{\mathrm{I}}^{(1)}K_{\mathrm{I}}^{(2)} + K_{\mathrm{II}}^{(1)}K_{\mathrm{II}}^{(2)}\right). \end{aligned} \tag{24}$$

Comparing Eqs. (16) and (24),

$$M^{(1,2)} = \frac{2}{E^*}\left[(K_{\mathrm{I}}^{(1)}K_{\mathrm{I}}^{(2)} + K_{\mathrm{II}}^{(1)}K_{\mathrm{II}}^{(2)})\right]. \tag{25}$$

The individual SIFs for the actual state can obtained by judiciously choosing the auxiliary state (state 2). For example, if state 2 is chosen to be state I, i.e., the mode-I near tip displacement and stress field is chosen as the auxiliary state, then $K_{\mathrm{I}}^{(2)} = 1$ and $K_{\mathrm{II}}^{(2)} = 0$. Hence, Eq. (25) can be reduced to

$$M^{(1,\mathrm{I})} = \frac{2K_{\mathrm{I}}^{(1)}}{E^*}, \tag{26}$$

from which

$$K_{\mathrm{I}}^{(1)} = \frac{M^{(1,\mathrm{I})}E^*}{2}. \tag{27}$$

Similarly, if state 2 is chosen to be state II, i.e., the mode-II near tip displacement and stress field is chosen as the auxiliary state, then $K_{\mathrm{I}}^{(2)} = 0$ and $K_{\mathrm{II}}^{(2)} = 1$. Following similar considerations,

$$K_{\mathrm{II}}^{(1)} = \frac{M^{(1,\mathrm{II})}E^*}{2}. \tag{28}$$

The interaction integrals $M^{(1,\mathrm{I})}$ and $M^{(1,\mathrm{II})}$ can be evaluated from Eq. (19). Eqs. (27) and (28) have been successfully used for calculating SIFs under various mixed-mode loading conditions [32–38].

3.2. Functionally graded materials

For non-homogeneous materials, even though the equilibrium and compatibility conditions are satisfied, the material gradient term of the second integrand of Eq. (12) does not vanish. So Eq. (12) reduces to a more general integral, henceforth referred to as the $\widetilde{J}$-integral [24], which is

$$\widetilde{J} = \int_A \left(\sigma_{ij}\frac{\partial u_i}{\partial x_1} - W\delta_{1j}\right)\frac{\partial q}{\partial x_j}\,\mathrm{d}A - \int_A \frac{1}{2}\varepsilon_{ij}\frac{\partial D_{ijkl}}{\partial x_1}\varepsilon_{kl}q\,\mathrm{d}A. \tag{29}$$

By comparing Eq. (29) to the classical J-integral (see Eq. (13)), the presence of material non-homogeneity results in the addition of the second domain integral. Although this integral is negligible for a path very close to the crack tip, it must be accounted for with relatively large integral domains, so that the $\widetilde{J}$-integral can be accurately calculated.

The $\widetilde{J}$-integral in Eq. (29) is actually the first component of the $\boldsymbol{J}^* = \{J_1^*, J_2^*\}^{\mathrm{T}}$ vector integral (i.e., J_1^*) proposed by Eischen [16]. Hence, $\widetilde{J}$ also represents the energy release rate of an elastic body. It is elementary to show that the $\widetilde{J}$-integral becomes *zero* for any closed contour in an uncracked homogeneous, as well as in non-homogeneous bodies, and therefore remains path independent when used in conjunction with cracks in FGM [16,44].

In order to derive interaction integral for FGMs, consider again actual (state 1), auxiliary (state 2), and superimposed (state S) equilibrium states. For the actual state, Eq. (29) can be directly invoked to represent the $\widetilde{J}$-integral. However, a more general form, such as Eq. (11), must be used for auxiliary and superimposed states. For example, the $\widetilde{J}$-integral for the superimposed state S can written as

$$\widetilde{J}^{(S)} = \int_A \left((\sigma_{ij}^{(1)} + \sigma_{ij}^{(2)})\frac{\partial(u_i^{(1)} + u_i^{(2)})}{\partial x_1} - W^{(S)}\delta_{1j}\right)\frac{\partial q}{\partial x_j}\,\mathrm{d}A + \int_A \frac{\partial}{\partial x_j}\left((\sigma_{ij}^{(1)} + \sigma_{ij}^{(2)})\frac{\partial(u_i^{(1)} + u_i^{(2)})}{\partial x_1} - W^{(S)}\delta_{1j}\right)q\,\mathrm{d}A. \tag{30}$$

Clearly, the evaluations of $\widetilde{J}^{(S)}$ and the resulting interaction integral depend on how the auxiliary field is defined. There are several options in choosing the auxiliary field. Two methods, developed in this study, are described in the following.

3.2.1. Method I: homogeneous auxiliary field

The method I involves selecting the auxiliary stress and displacement fields given by Eqs. (5)–(9) and calculating the auxiliary strain field from the symmetric gradient of the auxiliary displacement field. In this approach, the auxiliary stress and strain fields are related through a constant constitutive tensor evaluated at the crack tip. Hence, both equilibrium ($\partial\sigma_{ij}^{(2)}/\partial x_j = 0$) and compatibility ($\varepsilon_{ij}^{(2)} = \partial u_i^{(2)}/\partial x_j$) conditions are satisfied in the auxiliary state. However, the non-homogeneous constitutive relation of FGM is not strictly satisfied in the auxiliary state, which would introduce gradients of stress fields as extra terms in the interaction integral.

Using Eq. (20) and invoking both equilibrium and compatibility conditions, Eq. (30) can be further simplified to

$$\widetilde{J}^{(S)} = \int_A \left((\sigma_{ij}^{(1)} + \sigma_{ij}^{(2)}) \frac{\partial (u_i^{(1)} + u_i^{(2)})}{\partial x_1} - (W^{(1)} + W^{(2)} + W^{(1,2)}) \delta_{1j} \right) \frac{\partial q}{\partial x_j} \, \mathrm{d}A + \int_A \frac{1}{2} \left[- \varepsilon_{ij}^{(1)} \frac{\partial D_{ijkl}}{\partial x_1} \varepsilon_{kl}^{(1)} + \sigma_{ij}^{(1)} \frac{\partial \varepsilon_{ij}^{(2)}}{\partial x_1} - \frac{\partial \sigma_{ij}^{(2)}}{\partial x_1} \varepsilon_{ij}^{(1)} + \sigma_{ij}^{2} \frac{\partial \varepsilon_{ij}^{(1)}}{\partial x_1} - \frac{\partial \sigma_{ij}^{(1)}}{\partial x_1} \varepsilon_{ij}^{(2)} \right] q \, \mathrm{d}A. \tag{31}$$

By expanding Eq. (31),

$$\widetilde{J}^{(S)} = \widetilde{J}^{(1)} + \widetilde{J}^{(2)} + \widetilde{M}^{(1,2)}, \tag{32}$$

where

$$\widetilde{J}^{(1)} = \int_A \left[\sigma_{ij}^{(1)} \frac{\partial u_i^{(1)}}{\partial x_1} - W^{(1)} \delta_{1j} \right] \frac{\partial q}{\partial x_j} \, \mathrm{d}A - \int_A \frac{1}{2} \varepsilon_{ij}^{(1)} \frac{\partial D_{ijkl}}{\partial x_1} \varepsilon_{kl}^{(1)} q \, \mathrm{d}A, \tag{33}$$

$$\widetilde{J}^{(2)} = \int_A \left[\sigma_{ij}^{(2)} \frac{\partial u_i^{(2)}}{\partial x_1} - W^{(2)} \delta_{1j} \right] \frac{\partial q}{\partial x_j} \, \mathrm{d}A \tag{34}$$

are the $\widetilde{J}$-integrals for states 1 and 2, respectively, and

$$\widetilde{M}^{(1,2)} = \int_A \left[\sigma_{ij}^{(1)} \frac{\partial u_i^{(2)}}{\partial x_1} + \sigma_{ij}^{(2)} \frac{\partial u_i^{(1)}}{\partial x_1} - W^{(1,2)} \delta_{1j} \right] \frac{\partial q}{\partial x_j} \, \mathrm{d}A + \int_A \frac{1}{2} \left[\sigma_{ij}^{(1)} \frac{\partial \varepsilon_{ij}^{(2)}}{\partial x_1} - \frac{\partial \sigma_{ij}^{(2)}}{\partial x_1} \varepsilon_{ij}^{(1)} + \sigma_{ij}^{(2)} \frac{\partial \varepsilon_{ij}^{(1)}}{\partial x_1} - \frac{\partial \sigma_{ij}^{(1)}}{\partial x_1} \varepsilon_{ij}^{(2)} \right] q \, \mathrm{d}A \tag{35}$$

is the modified interaction integral for non-homogeneous materials.

3.2.2. Method II: non-homogeneous auxiliary field

The method II entails selecting the auxiliary stress and displacement fields given by Eqs. (5)–(9) and calculating the auxiliary strain field using the same spatially varying constitutive tensor of FGM. In this approach, the auxiliary stress field satisfies equilibrium ($\partial \sigma_{ij}^{(2)} / \partial x_j = 0$); however, the auxiliary strain field is not compatible with the auxiliary displacement field ($\varepsilon_{ij}^{(2)} \neq \partial u_i^{(2)} / \partial x_j$). If the auxiliary fields are not compatible, extra terms that will arise due to lack of compatibility should be taken into account while evaluating the interaction integral, even though they may not be sufficiently singular in the asymptotic limit to contribute to the value of the integral [45–47]. Hence, this method also introduces additional terms to the resulting interaction integral.

Following similar considerations, but using only equilibrium condition in the auxiliary state, Eq. (30) can also be simplified to

$$\widetilde{J}^{(S)} = \int_A \left((\sigma_{ij}^{(1)} + \sigma_{ij}^{(2)}) \frac{\partial (u_i^{(1)} + u_i^{(2)})}{\partial x_1} - (W^{(1)} + W^{(2)} + W^{(1,2)}) \delta_{1j} \right) \frac{\partial q}{\partial x_j} \, \mathrm{d}A + \int_A \left((\sigma_{ij}^{(1)} + \sigma_{ij}^{(2)}) \left(\frac{\partial^2 u_i^{(2)}}{\partial x_j \partial x_1} - \frac{\partial \varepsilon_{ij}^{(2)}}{\partial x_1} \right) - \frac{1}{2} (\varepsilon_{ij}^{(1)} + \varepsilon_{ij}^{(2)}) \frac{\partial D_{ijkl}}{\partial x_1} (\varepsilon_{kl}^{(1)} + \varepsilon_{kl}^{(2)}) \right) q \, \mathrm{d}A. \tag{36}$$

Comparing Eqs. (36) and (32),

$$\widetilde{J}^{(1)} = \int_A \left[\sigma_{ij}^{(1)} \frac{\partial u_i^{(1)}}{\partial x_1} - W^{(1)}\delta_{1j}\right] \frac{\partial q}{\partial x_j}\,\mathrm{d}A - \int_A \frac{1}{2}\varepsilon_{ij}^{(1)} \frac{\partial D_{ijkl}}{\partial x_1} \varepsilon_{kl}^{(1)} q\,\mathrm{d}A, \tag{37}$$

$$\widetilde{J}^{(2)} = \int_A \left[\sigma_{ij}^{(2)} \frac{\partial u_i^{(2)}}{\partial x_1} - W^{(2)}\delta_{1j}\right] \frac{\partial q}{\partial x_j}\,\mathrm{d}A + \int_A \left[\sigma_{ij}^{(2)} \left(\frac{\partial^2 u_i^{(2)}}{\partial x_j \partial x_1} - \frac{\partial \varepsilon_{ij}^{(2)}}{\partial x_1}\right) - \frac{1}{2}\varepsilon_{ij}^{(2)} \frac{\partial D_{ijkl}}{\partial x_1} \varepsilon_{kl}^{(2)}\right] q\,\mathrm{d}A \tag{38}$$

are the $\widetilde{J}$-integrals for states 1 and 2, respectively, and

$$\widetilde{M}^{(1,2)} = \int_A \left[\sigma_{ij}^{(1)} \frac{\partial u_i^{(2)}}{\partial x_1} + \sigma_{ij}^{(2)} \frac{\partial u_i^{(1)}}{\partial x_1} - W^{(1,2)}\delta_{1j}\right] \frac{\partial q}{\partial x_j}\,\mathrm{d}A + \int_A \left[\sigma_{ij}^{(1)} \left(\frac{\partial^2 u_i^{(2)}}{\partial x_j \partial x_1} - \frac{\partial \varepsilon_{ij}^{(2)}}{\partial x_1}\right) - \varepsilon_{ij}^{(1)} \frac{\partial D_{ijkl}}{\partial x_1} \varepsilon_{kl}^{(2)}\right] q\,\mathrm{d}A \tag{39}$$

is another modified interaction integral for non-homogeneous materials. Recently, Dolbow and Gosz [48] have also derived a path independent interaction integral which is the same as the one given by Eq. (39).

Note, for homogeneous materials, $\partial D_{ijkl}/\partial x_1 = 0$, $\varepsilon_{ij}^{(2)} = \partial u_i^{(2)}/\partial x_j$, $\sigma_{ij}^{(1)}\partial \varepsilon_{ij}^{(2)}/\partial x_1 = \partial \sigma_{ij}^{(2)}/\partial x_1 \varepsilon_{ij}^{(1)}$ and $\sigma_{ij}^{(2)}\partial \varepsilon_{ij}^{(1)}/\partial x_1 = \partial \sigma_{ij}^{(1)}/\partial x_1 \varepsilon_{ij}^{(2)}$, regardless of how the auxiliary field is defined. As a result, the $\widetilde{J}^{(1)}$, $\widetilde{J}^{(2)}$, and $\widetilde{M}^{(1,2)}$ integrals in methods I and II degenerate to their corresponding homogeneous solutions, as expected.

3.2.3. Stress-intensity factors

For linear-elastic solids, the $\widetilde{J}$-integral also represents the energy release rate and, hence,

$$\widetilde{J} = \frac{1}{E_{\mathrm{tip}}^*}(K_{\mathrm{I}}^2 + K_{\mathrm{II}}^2), \tag{40}$$

where E_{tip}^* is evaluated at the crack tip. Regardless of how the auxiliary fields are defined, Eq. (40) applied to states 1, 2, and S yields

$$\widetilde{J}^{(1)} = \frac{1}{E_{\mathrm{tip}}^*}(K_{\mathrm{I}}^{(1)^2} + K_{\mathrm{II}}^{(1)^2}), \tag{41}$$

$$\widetilde{J}^{(2)} = \frac{1}{E_{\mathrm{tip}}^*}(K_{\mathrm{I}}^{(2)^2} + K_{\mathrm{II}}^{(2)^2}) \tag{42}$$

and

$$\widetilde{J}^{(S)} = \widetilde{J}^{(1)} + \widetilde{J}^{(2)} + \frac{2}{E_{\mathrm{tip}}^*}(K_{\mathrm{I}}^{(1)}K_{\mathrm{I}}^{(2)} + K_{\mathrm{II}}^{(1)}K_{\mathrm{II}}^{(2)}). \tag{43}$$

Comparing Eq. (32) with Eq. (43),

$$\widetilde{M}^{(1,2)} = \frac{2}{E_{\mathrm{tip}}^*}\left[K_{\mathrm{I}}^{(1)}K_{\mathrm{I}}^{(2)} + K_{\mathrm{II}}^{(1)}K_{\mathrm{II}}^{(2)}\right]. \tag{44}$$

Following a similar procedure and judiciously choosing the intensity of the auxiliary state as described earlier, the SIFs for non-homogeneous materials can also be derived as

$$K_{\mathrm{I}}^{(1)} = \frac{\widetilde{M}^{(1,\mathrm{I})}E_{\mathrm{tip}}^*}{2} \tag{45}$$

and

$$K_{\mathrm{II}}^{(1)} = \frac{\widetilde{M}^{(1,\mathrm{II})} E^*_{\mathrm{tip}}}{2}, \tag{46}$$

where $\widetilde{M}^{(1,\mathrm{I})}$ and $\widetilde{M}^{(1,\mathrm{II})}$ are two modified interaction integrals for modes I and II, respectively, and can be evaluated using either Eq. (35) or Eq. (39). In contrast to existing methods, such as the J_k^*-integral method [16], there is no need to perform integration along the crack face of the discontinuity (e.g., in calculating J_2^*). Hence, the proposed methods are simpler than the J_k^*-integral method. Both methods developed in this study were used in performing numerical calculations, to be presented in a forthcoming section.

Note, Eqs. (45) and (46) are the result of a simple generalization of the interaction integral method for calculating fracture parameters in linear-elastic non-homogeneous materials. When both the elastic modulus and the Poisson's ratio have no spatial variation, $\widetilde{M}^{(1,2)} = M^{(1,2)}$. Consequently, Eqs. (45) and (46) degenerate into Eqs. (27) and (28), as expected.

4. Element-free Galerkin method

4.1. Moving least squares and meshless shape function

Consider a function $u(\boldsymbol{x})$ over a domain $\Omega \subseteq \Re^2$. Let $\Omega_x \subseteq \Omega$ denote a sub-domain describing the neighborhood of a point $\boldsymbol{x} \in \Re^K$ located in Ω. According to the MLS [49] method, the approximation $u^h(\boldsymbol{x})$ of $u(\boldsymbol{x})$ is

$$u^h(\boldsymbol{x}) = \sum_{i=1}^{m} p_i(\boldsymbol{x}) a_i(\boldsymbol{x}) = \boldsymbol{p}^{\mathrm{T}}(\boldsymbol{x}) \boldsymbol{a}(\boldsymbol{x}), \tag{47}$$

where $\boldsymbol{p}^{\mathrm{T}}(\boldsymbol{x}) = \{p_1(\boldsymbol{x}), p_2(\boldsymbol{x}), \ldots, p_m(\boldsymbol{x})\}$ is a vector of complete basis functions of order m and $\boldsymbol{a}(\boldsymbol{x}) = \{a_1(\boldsymbol{x}), a_2(\boldsymbol{x}), \ldots, a_m(\boldsymbol{x})\}$ is a vector of unknown parameters that depend on $\boldsymbol{x}$. For example, in the x_1–x_2 coordinate system,

$$\boldsymbol{p}^{\mathrm{T}}(\boldsymbol{x}) = \{1, x_1, x_2\}, \quad m = 3 \tag{48}$$

and

$$\boldsymbol{p}^{\mathrm{T}}(\boldsymbol{x}) = \{1, x_1, x_2, x_1^2, x_1 x_2, x_2^2\}, \quad m = 6 \tag{49}$$

are linear and quadratic basis functions, respectively, and are commonly used in solid mechanics. The basis functions are not required to be polynomials. When solving problems involving cracks, a convenient way of capturing $1/\sqrt{r}$ stress-singularity in linear-elastic fracture mechanics (LEFM) is by using [32,37]

$$\boldsymbol{p}^{\mathrm{T}}(\boldsymbol{x}) = \left\{1, x_1, x_2, \sqrt{r}\cos(\theta/2), \sqrt{r}\sin(\theta/2), \sqrt{r}\sin(\theta/2)\sin\theta, \sqrt{r}\cos(\theta/2)\sin\theta\right\}, \quad m = 7, \tag{50}$$

where r and θ are polar coordinates with the crack tip as the origin.

In Eq. (47), the coefficient vector $\boldsymbol{a}(\boldsymbol{x})$ is determined by minimizing a weighted discrete $\mathscr{L}_2$ norm, defined as

$$J(\boldsymbol{x}) = \sum_{I=1}^{n} w_I(\boldsymbol{x}) [\boldsymbol{p}^{\mathrm{T}}(\boldsymbol{x}_I)\boldsymbol{a}(\boldsymbol{x}) - d_I]^2 = [\boldsymbol{P}\boldsymbol{a}(\boldsymbol{x}) - \boldsymbol{d}]^{\mathrm{T}} \boldsymbol{W} [\boldsymbol{P}\boldsymbol{a}(\boldsymbol{x}) - \boldsymbol{d}], \tag{51}$$

where $\boldsymbol{x}_I$ denotes the coordinates of node I, $\boldsymbol{d}^{\mathrm{T}} = \{d_1, d_2, \ldots, d_n\}$ with d_I representing the nodal parameter for node I, $\boldsymbol{W} = \mathrm{diag}[w_1(\boldsymbol{x}), w_2(\boldsymbol{x}), \ldots, w_n(\boldsymbol{x})]$ with $w_I(\boldsymbol{x})$ being the weight function associated with node I, such that $w_I(\boldsymbol{x}) > 0$ for all $\boldsymbol{x}$ in the support Ω_x of $w_I(\boldsymbol{x})$ and *zero* otherwise, n is the number of nodes in Ω_x for which $w_I(\boldsymbol{x}) > 0$, and

$$\boldsymbol{P} = \begin{bmatrix} \boldsymbol{p}^{\mathrm{T}}(\boldsymbol{x}_1) \\ \boldsymbol{p}^{\mathrm{T}}(\boldsymbol{x}_2) \\ \vdots \\ \boldsymbol{p}^{\mathrm{T}}(\boldsymbol{x}_n) \end{bmatrix} \in \mathscr{L}(\Re^n \times \Re^m). \tag{52}$$

A number of weight functions are available in the literature [32–38]. In this study, a weight function proposed by Rao and Rahman [32] was used, and is expressed as

$$w_I(\boldsymbol{x}) = \begin{cases} \dfrac{\left(1+\beta^2 \dfrac{z_I^2}{z_{mI}^2}\right)^{-(1+\beta)/2} - (1+\beta^2)^{-(1+\beta)/2}}{1-(1+\beta^2)^{-(1+\beta)/2}} & z_I \leqslant z_{mI}, \\ 0 & z_I > z_{mI}, \end{cases} \tag{53}$$

where β is a parameter controlling the shape of the weight function, $z_I = \|\boldsymbol{x} - \boldsymbol{x}_I\|$ is the distance from a sample point $\boldsymbol{x}$ to a node $\boldsymbol{x}_I$, and z_{mI} is the domain of influence of node I. The stationarity of $J(\boldsymbol{x})$ with respect to $\boldsymbol{a}(\boldsymbol{x})$ yields

$$\boldsymbol{A}(\boldsymbol{x})\boldsymbol{a}(\boldsymbol{x}) = \boldsymbol{C}(\boldsymbol{x})\boldsymbol{d}, \tag{54}$$

where

$$\boldsymbol{A}(\boldsymbol{x}) = \sum_{I=1}^{n} w_I(\boldsymbol{x})\boldsymbol{p}(\boldsymbol{x}_I)\boldsymbol{p}^{\mathrm{T}}(\boldsymbol{x}_I) = \boldsymbol{P}^{\mathrm{T}}\boldsymbol{W}\boldsymbol{P}, \tag{55}$$

$$\boldsymbol{C}(\boldsymbol{x}) = [w_1(\boldsymbol{x})\boldsymbol{p}(\boldsymbol{x}_1), \ldots, w_n(\boldsymbol{x})\boldsymbol{p}(\boldsymbol{x}_n)] = \boldsymbol{P}^{\mathrm{T}}\boldsymbol{W}. \tag{56}$$

Solving for $\boldsymbol{a}(\boldsymbol{x})$ in Eq. (54) and then substituting into Eq. (47) yields

$$u^h(\boldsymbol{x}) = \sum_{I=1}^{n} \Phi_I(\boldsymbol{x})d_I = \boldsymbol{\Phi}^{\mathrm{T}}(\boldsymbol{x})\boldsymbol{d}, \tag{57}$$

where

$$\boldsymbol{\Phi}^{\mathrm{T}}(\boldsymbol{x}) = \{\Phi_1(\boldsymbol{x}), \Phi_2(\boldsymbol{x}), \ldots, \Phi_n(\boldsymbol{x})\} = \boldsymbol{p}^{\mathrm{T}}(\boldsymbol{x})\boldsymbol{A}^{-1}(\boldsymbol{x})\boldsymbol{C}(\boldsymbol{x}) \tag{58}$$

is a vector with its Ith component,

$$\Phi_I(\boldsymbol{x}) = \sum_{j=1}^{m} p_j(\boldsymbol{x})[\boldsymbol{A}^{-1}(\boldsymbol{x})\boldsymbol{C}(\boldsymbol{x})]_{jI}, \tag{59}$$

representing the shape function of the MLS approximation corresponding to node I. The partial derivatives of $\Phi_I(\boldsymbol{x})$ can also be obtained as

$$\Phi_{I,i}(\boldsymbol{x}) = \sum_{j=1}^{m} \{p_{j,i}(\boldsymbol{A}^{-1}\boldsymbol{C})_{jI} + p_j(\boldsymbol{A}_{,i}^{-1}\boldsymbol{C} + \boldsymbol{A}^{-1}\boldsymbol{C}_{,i})_{jI}\}, \tag{60}$$

where $\boldsymbol{A}_{,i}^{-1} = -\boldsymbol{A}^{-1}\boldsymbol{A}_{,i}\boldsymbol{A}^{-1}$ and $(\,)_{,i} = \dfrac{\partial(\,)}{\partial x_i}$.

Note that the MLS/meshless shape function $\Phi_I(\boldsymbol{x})$ strongly depends on the type of basis functions used. For problem involving cracks, the enriched basis function, such as the one in Eq. (50), is required to produce stress singularity at the crack tip. However, this singularity field is only local to the crack tip. Therefore, it is unnecessary to use an enriched basis for the entire domain. In that case, a hybrid approach involving an enriched basis close to the crack tip and a regular basis far away from the crack tip can be used. For example, if $\Phi_I^{\mathrm{r}}(\boldsymbol{x})$ and $\Phi_I^{\mathrm{e}}(\boldsymbol{x})$ denote two resulting shape functions using regular (e.g., Eqs. (48) or

(49)) and enriched (e.g., Eq. (50)) basis functions, respectively, the effective shape function due to coupling can be expressed by [32,37]

$$\Phi_I(\boldsymbol{x}) = R\Phi_I^{\mathrm{e}}(\boldsymbol{x}) + (1-R)\Phi_I^{\mathrm{r}}(\boldsymbol{x}), \tag{61}$$

where R is an appropriate ramp function that is equal to *unity* on the enriched boundary of the coupling region and *zero* on the regular side of the coupling region.

4.2. Variational formulation and discretization

For small displacements in two-dimensional, isotropic, and linear-elastic solids, the equilibrium equations and boundary conditions are

$$\nabla \cdot \boldsymbol{\sigma} + \boldsymbol{b} = 0 \quad \text{in } \Omega \tag{62}$$

and

$$\begin{aligned} &\boldsymbol{\sigma}\cdot\boldsymbol{n} = \bar{\boldsymbol{t}} \quad \text{on } \Gamma_t \text{ (natural boundary conditions)},\\ &\boldsymbol{u} = \bar{\boldsymbol{u}} \quad \text{on } \Gamma_u \text{ (essential boundary conditions)}, \end{aligned} \tag{63}$$

respectively, where $\boldsymbol{\sigma} = \boldsymbol{D}(\boldsymbol{x})\boldsymbol{\epsilon}$ is the stress vector, $\boldsymbol{D}(\boldsymbol{x})$ is the material property matrix, $\boldsymbol{\epsilon} = \nabla_{\mathrm{s}}\boldsymbol{u}$ is the strain vector, $\boldsymbol{u}$ is the displacement vector, $\boldsymbol{b}$ is the body force vector, $\bar{\boldsymbol{t}}$ and $\bar{\boldsymbol{u}}$ are the vectors of prescribed surface tractions and displacements, respectively, $\boldsymbol{n}$ is a unit normal to the domain, Ω, Γ_t and Γ_u are the portions of boundary Γ where tractions and displacements are prescribed, $\nabla^{\mathrm{T}} = \{\partial/\partial x_1, \partial/\partial x_2\}$ is the vector of gradient operators, and $\nabla_{\mathrm{s}}\boldsymbol{u}$ is the symmetric part of $\nabla\boldsymbol{u}$. The variational or weak form of Eqs. (62) and (63) is

$$\int_\Omega \boldsymbol{\sigma}^{\mathrm{T}}\,\delta\boldsymbol{\epsilon}\,\mathrm{d}\Omega - \int_\Omega \boldsymbol{b}^{\mathrm{T}}\,\delta\boldsymbol{u}\,\mathrm{d}\Omega - \int_\Omega \bar{\boldsymbol{t}}^{\mathrm{T}}\,\delta\boldsymbol{u}\,\mathrm{d}\Gamma + \sum_{\boldsymbol{x}_K\in\Gamma_u} \boldsymbol{f}^{\mathrm{T}}(\boldsymbol{x}_K)\delta\boldsymbol{u}(\boldsymbol{x}_K) + \sum_{\boldsymbol{x}_K\in\Gamma_u} \delta\boldsymbol{f}^{\mathrm{T}}(\boldsymbol{x}_K)[\boldsymbol{u}(\boldsymbol{x}_K) - \bar{\boldsymbol{u}}(\boldsymbol{x}_K)] = 0, \tag{64}$$

where $\boldsymbol{f}^{\mathrm{T}}(\boldsymbol{x}_K)$ is the vector of reaction forces at the constrained node K on Γ_u and δ denotes the variation operator. From Eq. (57), the MLS approximation of $\boldsymbol{u}(\boldsymbol{x}) = \{u_1(\boldsymbol{x}), u_2(\boldsymbol{x})\}^{\mathrm{T}}$ in two dimensions is

$$\boldsymbol{u}^h(\boldsymbol{x}) = \boldsymbol{\Phi}^{\mathrm{T}}\boldsymbol{d}, \tag{65}$$

where

$$\boldsymbol{\Phi}^{\mathrm{T}}(\boldsymbol{x}) = \begin{bmatrix} \Phi_1(\boldsymbol{x}) & 0 & \Phi_2(\boldsymbol{x}) & 0 & \cdots & \Phi_N(\boldsymbol{x}) & 0 \\ 0 & \Phi_1(\boldsymbol{x}) & 0 & \Phi_2(\boldsymbol{x}) & \cdots & 0 & \Phi_N(\boldsymbol{x}) \end{bmatrix}, \tag{66}$$

$$\boldsymbol{d} = \begin{Bmatrix} d_1^1 \\ d_1^2 \\ d_2^1 \\ d_2^2 \\ \vdots \\ d_N^1 \\ d_N^2 \end{Bmatrix} \tag{67}$$

is the vector of nodal parameters or generalized displacements, and N is the total number of nodal points in Ω. Applying Eqs. (65)–(67) to the discretization of Eq. (64) yields

$$\begin{bmatrix} \boldsymbol{k} & \boldsymbol{G} \\ \boldsymbol{G}^{\mathrm{T}} & 0 \end{bmatrix} \begin{Bmatrix} \boldsymbol{d} \\ \boldsymbol{f}_R \end{Bmatrix} = \begin{Bmatrix} \boldsymbol{f}^{\mathrm{ext}} \\ \boldsymbol{g} \end{Bmatrix}, \tag{68}$$

where

$$\boldsymbol{k} = \begin{bmatrix} \boldsymbol{k}_{11} & \boldsymbol{k}_{12} & \cdots & \boldsymbol{k}_{1N} \\ \boldsymbol{k}_{21} & \boldsymbol{k}_{22} & \cdots & \boldsymbol{k}_{2N} \\ \vdots & \vdots & \vdots & \vdots \\ \boldsymbol{k}_{N1} & \boldsymbol{k}_{N2} & \cdots & \boldsymbol{k}_{NN} \end{bmatrix} \in \mathscr{L}(\Re^{2N} \times \Re^{2N}) \tag{69}$$

is the stiffness matrix with

$$\boldsymbol{k}_{IJ} = \int_{\Omega} \boldsymbol{B}_I^{\mathrm{T}} \boldsymbol{D} \boldsymbol{B}_J \, \mathrm{d}\Omega \in \mathscr{L}(\Re^2 \times \Re^2), \tag{70}$$

$$\boldsymbol{G}^{\mathrm{T}} = \begin{bmatrix} \Phi_1(\boldsymbol{x}_1) & 0 & \Phi_1(\boldsymbol{x}_2) & 0 & \cdots & \Phi_1(\boldsymbol{x}_N) & 0 \\ 0 & \Phi_1(\boldsymbol{x}_1) & 0 & \Phi_1(\boldsymbol{x}_2) & \cdots & 0 & \Phi_1(\boldsymbol{x}_N) \\ \Phi_2(\boldsymbol{x}_1) & 0 & \Phi_2(\boldsymbol{x}_2) & 0 & \cdots & \Phi_2(\boldsymbol{x}_N) & 0 \\ \cdots & \Phi_2(\boldsymbol{x}_1) & 0 & \Phi_2(\boldsymbol{x}_2) & \cdots & 0 & \Phi_2(\boldsymbol{x}_N) \\ \vdots & \vdots & \vdots & \vdots & \vdots & \vdots & \vdots \\ \Phi_L(\boldsymbol{x}_1) & 0 & \Phi_L(\boldsymbol{x}_2) & 0 & \cdots & \Phi_L(\boldsymbol{x}_N) & 0 \\ 0 & \Phi_L(\boldsymbol{x}_1) & 0 & \Phi_L(\boldsymbol{x}_2) & \cdots & 0 & \Phi_L(\boldsymbol{x}_N) \end{bmatrix} \in \mathscr{L}(\Re^{2L} \times \Re^{2N}) \tag{71}$$

is a matrix comprising shape function values of nodes at which the displacement boundary conditions are prescribed, L is the total number of nodes on Γ_u,

$$\boldsymbol{f}_R = \begin{Bmatrix} \boldsymbol{f}(\boldsymbol{x}_{K_1}) \\ \boldsymbol{f}(\boldsymbol{x}_{K_2}) \\ \vdots \\ \boldsymbol{f}(\boldsymbol{x}_{K_L}) \end{Bmatrix} \in \Re^{2L} \tag{72}$$

is the vector of reaction forces on Γ_u,

$$\boldsymbol{f}^{\mathrm{ext}} = \int_{\Omega} \boldsymbol{\Phi}^{\mathrm{T}} \boldsymbol{b} \, \mathrm{d}\Omega + \int_{\Gamma_t} \boldsymbol{\Phi}^{\mathrm{T}} \bar{\boldsymbol{t}} \, \mathrm{d}\Gamma \in \Re^{2N} \tag{73}$$

is the force vector, and

$$\boldsymbol{g} = \begin{Bmatrix} \bar{\boldsymbol{u}}(\boldsymbol{x}_{K_1}) \\ \bar{\boldsymbol{u}}(\boldsymbol{x}_{K_2}) \\ \vdots \\ \bar{\boldsymbol{u}}(\boldsymbol{x}_{K_L}) \end{Bmatrix} \in \Re^{2L} \tag{74}$$

is the vector of prescribed displacements on Γ_u. In Eq. (70),

$$\boldsymbol{B}_I = \begin{bmatrix} \Phi_{I,1} & 0 \\ 0 & \Phi_{I,2} \\ \Phi_{I,2} & \Phi_{I,1} \end{bmatrix} \tag{75}$$

and

$$\boldsymbol{D}(\boldsymbol{x}) = \begin{cases} \dfrac{E(\boldsymbol{x})}{1-v(\boldsymbol{x})^2} \begin{bmatrix} 1 & v(\boldsymbol{x}) & 0 \\ v(\boldsymbol{x}) & 1 & 0 \\ 0 & 0 & \dfrac{1-v(\boldsymbol{x})}{2} \end{bmatrix} & \text{for plane stress,} \\ \dfrac{E(\boldsymbol{x})}{[1+v(\boldsymbol{x})][1-2v(\boldsymbol{x})]} \begin{bmatrix} 1-v(\boldsymbol{x}) & v(\boldsymbol{x}) & 0 \\ v(\boldsymbol{x}) & 1-v(\boldsymbol{x}) & 0 \\ 0 & 0 & \dfrac{1-2v(\boldsymbol{x})}{2} \end{bmatrix} & \text{for plane strain} \end{cases} \tag{76}$$

is the elasticity matrix.

In order to perform numerical integration in Eqs. (70) and (73), a background mesh is required, which can be independent of the arrangement of meshless nodes. However, in this study, the nodes of the background mesh were assumed to coincide with the meshless nodes. Standard Gaussian quadrature was used to evaluate the integrals for assembling the stiffness matrix and force vector. In FGM, the elasticity matrix $\boldsymbol{D}(\boldsymbol{x})$ is spatially dependent because of functionally distributed $E(\boldsymbol{x})$ and/or $v(\boldsymbol{x})$. There are two approaches to incorporate the material gradation effects on $\boldsymbol{k}$. In the first approach, meshless shape functions and nodal values of material properties can approximate the values of material properties at Gauss points. In the second approach, the values of material properties at Gauss points can be evaluated directly using Eqs. (1) and (2). In this study, the second approach was adopted for generating the stiffness matrix and force vector. In general, a 4×4 quadrature rule is adequate, except in the cells surrounding a high stress gradient (e.g., near a crack tip), where an 8×8 quadrature rule is suggested.

In solving for $\boldsymbol{d}$, the essential boundary conditions must be enforced. The lack of Kronecker delta properties in meshless shape functions presents some difficulty in imposing essential boundary conditions in EFGM. Nevertheless, several methods are currently available for enforcing essential boundary conditions. In this study, a full transformation method [32,50] was used to evaluate the SIFs in FGM.

It should be noted that the generalized displacement vector $\boldsymbol{d}$ represents the nodal parameters, and not the actual displacements at the meshless nodes. Let

$$\hat{\boldsymbol{d}} = \begin{Bmatrix} \boldsymbol{u}^h(\boldsymbol{x}_1) \\ \boldsymbol{u}^h(\boldsymbol{x}_2) \\ \vdots \\ \boldsymbol{u}^h(\boldsymbol{x}_N) \end{Bmatrix} = \begin{Bmatrix} u_1^h(\boldsymbol{x}_1) \\ u_2^h(\boldsymbol{x}_1) \\ u_1^h(\boldsymbol{x}_2) \\ u_2^h(\boldsymbol{x}_2) \\ \vdots \\ u_1^h(\boldsymbol{x}_N) \\ u_2^h(\boldsymbol{x}_N) \end{Bmatrix} \in \Re^{2N}, \tag{77}$$

represent the vector of nodal displacements. From Eq. (65),

$$\hat{\boldsymbol{d}} = \boldsymbol{\Lambda}\boldsymbol{d}, \tag{78}$$

where

$$\boldsymbol{\Lambda} = \begin{bmatrix} \boldsymbol{\Phi}^{\mathrm{T}}(\boldsymbol{x}_1) \\ \boldsymbol{\Phi}^{\mathrm{T}}(\boldsymbol{x}_2) \\ \vdots \\ \boldsymbol{\Phi}^{\mathrm{T}}(\boldsymbol{x}_N) \end{bmatrix} \in \mathscr{L}\left(\Re^{2N} \times \Re^{2N}\right) \tag{79}$$

is the transformation matrix. Hence, $\hat{\boldsymbol{d}}$ can be easily calculated when $\boldsymbol{d}$ is known.

5. Numerical examples

EFGM with the newly modified interaction integrals (methods I and II) developed in this study was applied to evaluate the SIFs of cracks in FGMs. Both single-(mode-I) and mixed-mode (modes I and II) conditions were considered and five examples are presented here. In all five examples, the elastic modulus was assumed to vary spatially, while the Poisson's ratio was held constant. This is a reasonable assumption, since variation of the Poisson's ratio is usually small compared to that of the elastic modulus. The values of $\lambda = 1$ and $\beta = 4$ were used for meshless analysis in all examples. A fully enriched basis function was used in the first four examples. In the last example a hybrid enrichment of the basis function was adopted using a fully enriched basis function for a small region close to the two crack tip regions, and by using a linear basis function for the rest of the domain. For numerical integration, an 8×8 Gauss quadrature rule was used in all examples for all cells of the background mesh.

5.1. Example 1: edge-cracked plate under mode-I

Consider an edge-cracked plate with length $L = 8$ units, width $W = 1$ unit, and crack length a, as shown in Fig. 2(a). Three loading conditions including the uniform fixed grip loading (constant strain), the membrane loading (constant tensile stress), and pure bending (linear stress) were considered. Fig. 2(a)–(c) shows the schematics of the three loading conditions. The elastic modulus was assumed to follow an exponential function, given by

$$E(x_1) = E_1 \exp(\eta x_1), \quad 0 \leqslant x_1 \leqslant W, \tag{80}$$

where $E_1 = E(0)$, $E_2 = E(W)$, and $\eta = \ln(E_2/E_1)$. In Eq. (80), E_1 and η are two independent material parameters that characterize the elastic modulus variation. The following numerical values were used: $E_1 = 1$ unit, $E_2/E_1 = \exp(\eta) = 0.1$, 0.2, 5, and 10, and $a/W = 0.2$, 0.3, 0.4, 0.5 and 0.6. The Poisson's ratio was held constant with $v = 0.3$. A plane strain condition was assumed. Erdogan and Wu [51], who originally studied this example, also provided a theoretical solution.

Due to the symmetry of geometry and load, only half of the plate, as shown in Fig. 2(d), was analyzed by EFGM. The EFGM model consists of a total of 368 nodes, which includes 341 regularly distributed nodes and 27 nodes in three rings around the crack tip. A typical nodal distribution for the case in which $a/W = 0.5$ is shown in Fig. 2(e). An enlarged view of nodal refinement around the crack tip is depicted in Fig. 2(f). The domain of the plate was divided by 30×10 rectangular cells with their nodes coincident with 341 regularly distributed meshless nodes, used solely for numerical integration. The proposed method I with a domain size $2b \times b$ ($b = 0.10$ units), shown in Fig. 2(d), was used for evaluating the $\widetilde{M}^{(1,2)}$-integral.

Tables 1–3 show normalized mode-I SIFs $K_{\mathrm{I}}/\sigma_0\sqrt{\pi a}$, $K_{\mathrm{I}}/\sigma_{\mathrm{t}}\sqrt{\pi a}$, and $K_{\mathrm{I}}/\sigma_{\mathrm{b}}\sqrt{\pi a}$ for fixed grip, membrane loading, and bending, respectively, where $\sigma_0 = E_1\varepsilon_0/(1-v^2)$, $\varepsilon_0 = 1$, $\sigma_{\mathrm{t}} = \sigma_{\mathrm{b}} = 1$ unit. The results show that the predicted SIF obtained by the proposed EFGM (method I) agree very well with the analytical results of Erdogan and Wu [51], for all three types of loading and for various combinations of E_2/E_1 and a/W ratios. In addition, Tables 1–3 include some numerical results by Kim and Paulino [30] and/or Chen et al. [52].

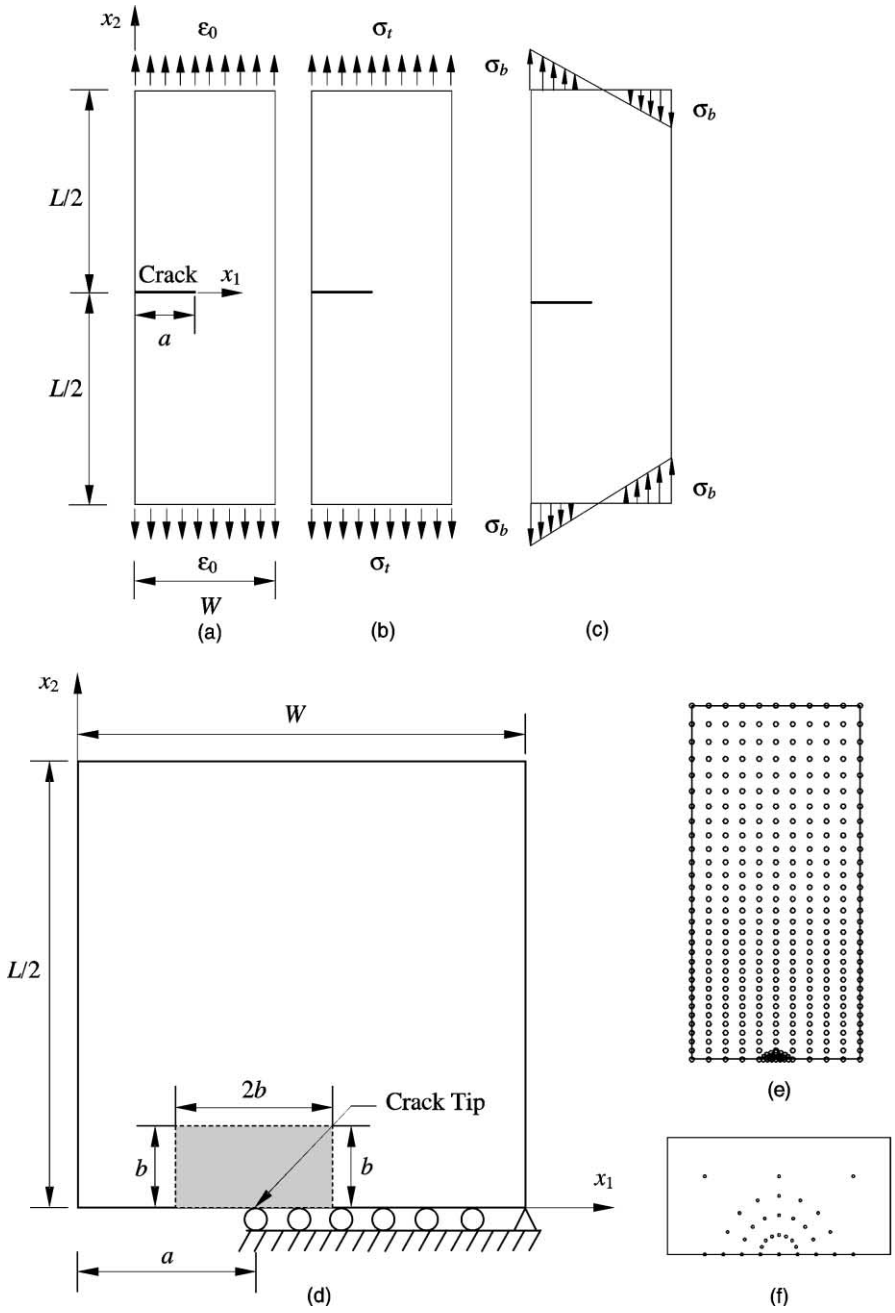

Fig. 2. Edge-cracked plate under mode-I loading: (a) geometry and loads for fixed grip loading; (b) membrane loading; (c) bending; (d) half model; (e) meshless discretization of half model (368 nodes) and extra nodal refinements around crack tip; and (f) extra nodal refinements around crack tip.

The present EFGM results correlate satisfactorily with the FEM results by Kim and Paulino [30], which are only reported for membrane loading and bending. The EFGM results of Chen et al. [52], which are re-

Table 1
Normalized mode-I SIF for an edge-cracked plate under fixed grip loading

Method	E_2/E_1	$\frac{K_I}{\sigma_0\sqrt{\pi a}}$				
		$a/W = 0.2$	$a/W = 0.3$	$a/W = 0.4$	$a/W = 0.5$	$a/W = 0.6$
Proposed method-I $[\widetilde{M}^{(1,2)}]$	0.1	1.3118	1.5191	1.8241	2.2800	3.0100
	0.2	1.3186	1.5460	1.8837	2.3966	3.2274
	5	1.4835	1.9161	2.5819	3.6698	5.5708
	10	1.5557	2.0724	2.8789	4.2234	6.6266
Erdogan and Wu [51]	0.1	1.2963	1.5083	1.8246	2.3140	3.1544
	0.2	1.3058	1.5330	1.8751	2.4031	3.2981
	5	1.4946	1.9118	2.5730	3.6573	5.5704
	10	1.5740	2.0723	2.8736	4.2140	6.6319
Chen et al. [52]	0.1	1.2961	1.4919	1.7962	2.2594	3.0544
	0.2	1.3145	1.5283	1.8659	2.3877	3.2910
	5	1.5414	1.9499	2.6238	3.7429	5.7936
	10	1.6296	2.1206	2.9398	4.3272	6.9171

Table 2
Normalized mode-I SIF for an edge-cracked plate under membrane loading

Method	E_2/E_1	$\frac{K_I}{\sigma_t\sqrt{\pi a}}$				
		$a/W = 0.2$	$a/W = 0.3$	$a/W = 0.4$	$a/W = 0.5$	$a/W = 0.6$
Proposed method-I $[\widetilde{M}^{(1,2)}]$	0.1	1.3374	1.8976	2.5938	3.5472	4.9956
	0.2	1.4193	1.8668	2.4657	3.3297	4.6905
	5	1.1269	1.3754	1.7576	2.3772	3.4478
	10	0.9958	1.2343	1.5980	2.1889	3.2167
Erdogan and Wu [51]	0.1	1.2965	1.8581	2.5699	3.5701	5.1880
	0.2	1.3956	1.8395	2.4436	3.3266	4.7614
	5	1.1318	1.3697	1.7483	2.3656	3.4454
	10	1.0019	1.2291	1.5884	2.1762	3.2124
Chen et al. [52]	0.1	1.3193	1.8642	2.5588	3.5213	5.0726
	0.2	1.4188	1.8497	2.4486	3.3234	4.7860
	5	1.1622	1.3899	1.7746	2.4125	3.5736
	10	1.0324	1.2499	1.6146	2.2234	3.3371
Kim and Paulino [30] (J_1^*)	0.1	1.2840	1.8460	2.5440	3.4960	4.9620
	0.2	1.3900	1.8310	2.4310	3.2920	4.6690
	5	1.1320	1.3700	1.7490	2.3660	3.4480
	10	1.0030	1.2280	1.5880	2.1750	3.2120

ported for fixed grip and membrane loading, also agree reasonably well with the present EFGM results. It is worth noting that the EFGM results of Chen et al. [52] are based on a linear basis function and the classical J-integral for homogeneous materials.

5.2. Example 2: three-point bend specimen under mode-I

Consider a three-point bend specimen with length $L = 54$ units, depth $2H = 10$ units, and thickness $t = 1$ unit, as shown in Fig. 3(a). A concentrated load $P = 1$ unit was applied at the middle of the beam of span

Table 3
Normalized mode-I SIF for an edge-cracked plate under bending

Method	E_2/E_1	$\frac{K_I}{\sigma_b\sqrt{\pi a}}$				
		$a/W = 0.2$	$a/W = 0.3$	$a/W = 0.4$	$a/W = 0.5$	$a/W = 0.6$
Proposed method-I $[\tilde{M}^{(1,2)}]$	0.1	1.9029	1.8747	1.9539	2.1547	2.5484
	0.2	1.5976	1.6109	1.7150	1.9322	2.3347
	5	0.6865	0.7830	0.9310	1.1666	1.5626
	10	0.5635	0.6637	0.8120	1.0447	1.4340
Erdogan and Wu [51]	0.1	1.9040	1.8859	1.9778	2.2151	2.7170
	0.2	1.5952	1.6122	1.7210	1.9534	2.4037
	5	0.6871	0.7778	0.9236	1.1518	1.5597
	10	0.5648	0.6588	0.8043	1.0350	1.4286
Kim and Paulino [30] (J_1^*)	0.1	1.8880	1.8640	1.9430	2.1450	2.5530
	0.2	1.5880	1.6010	1.7060	1.9250	2.3410
	5	0.6870	0.7780	0.9240	1.1580	1.5610
	10	0.5650	0.6590	0.8040	1.0350	1.4290

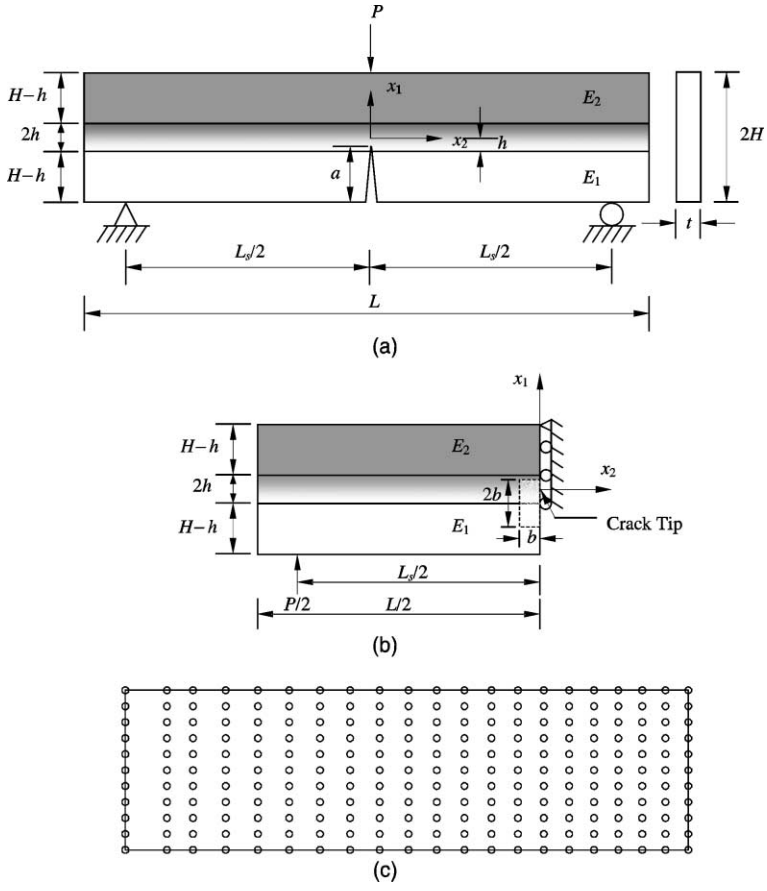

Fig. 3. Three-point bend specimen under mode-I loading: (a) geometry and loads; (b) half model; and (c) meshless discretization of half model (231 nodes).

$L_S = 50$ units and two supports were symmetrically placed with respect to an edge crack of length a. In the depth direction, the beam consists of $2h$ units deep FGM sandwiched between two distinct homogeneous materials, each of which has depth $H - h$. If E_1 and E_2 represent the elastic moduli of the bottom and top layers, the elastic modulus of the FGM layer varies linearly, with the end values matching the properties of the bottom and top layers. Mathematically, such a variation can be defined as

$$E(x_1) = \begin{cases} E_2, & x_1 \geqslant h, \\ \dfrac{E_1 + E_2}{2} + \dfrac{E_2 - E_1}{2h}, & -h \leqslant x_1 \leqslant h, \\ E_1, & x_1 \leqslant -h, \end{cases} \tag{81}$$

where E_1, E_2 and $2h$ are material parameters. The following numerical values were chosen: $2h = 1$ unit, $E_1 = 1$ unit, and $E_2/E_1 = 0.05$, 0.1, 0.2, 0.5, 1, 2, 5, 10, and 20. For each E_2/E_1 ratio, three different crack lengths with $a/2H = 0.45$, 0.5 and 0.55 were selected such that the crack tips were either at the middle of the FGM layer ($a/2H = 0.5$) or at the material interfaces ($a/2H = 0.45$ or 0.55). The Poisson's ratio was held constant with $v = 0.3$. A plane stress condition was assumed.

Due to symmetric geometry and loading with respect to the crack, only a half model of the beam, as shown in Fig. 3(b), was analyzed. Fig. 3(c) shows the details of the meshless discretization consisting of 231 nodes for the half beam model. The domain of the plate was divided by 20×10 rectangular cells with their nodes coincident to the meshless nodes only for numerical integration. The $\widetilde{M}^{(1,2)}$-integral was evaluated using method I over a domain size $2b \times b$ with $b = 0.5$ units, as shown in Fig. 3(b).

Table 4 shows the predicted normalized mode-I SIF $K_I\sqrt{H}/P$, obtained by the proposed EFGM (method I) for various combinations of E_2/E_1 and $a/2H$. Also presented in Table 4 are the corresponding FEM results by Kim and Paulino [30]. The SIFs by EFGM are in good agreement with the FEM results. Although not explicitly presented here, the graphical results of Gu et al. [24] can also be shown to agree well with the present EFGM results.

5.3. Example 3: composite strip under mode-I

Consider the square composite strip configuration studied by Eischen [16] with size $L = 1$ unit, $2h_1 = 0.6$ units and $2h_2 = 0.4$ units, as shown in Fig. 4(a). A crack of length $a = 0.4$ units is located on the line $x_2 = 0$. The Poisson's ratio was held constant at $v = 0.3$. The elastic modulus was assumed to vary smoothly according to a hyperbolic tangent function, given by

Table 4
Normalized mode-I SIF for a three-point bend specimen

E_2/E_1	$\frac{K_I\sqrt{H}}{P}$					
	$a/2H = 0.45$		$a/2H = 0.5$		$a/2H = 0.55$	
	Proposed method-I $[\widetilde{M}^{(1,2)}]$	Kim and Paulino [30] (J_1^*)	Proposed method-I $[\widetilde{M}^{(1,2)}]$	Kim and Paulino [30] (J_1^*)	Proposed method-I $[\widetilde{M}^{(1,2)}]$	Kim and Paulino [30] (J_1^*)
0.05	32.99	33.04	31.53	31.12	15.50	15.21
0.1	23.61	23.47	23.96	23.92	13.40	13.73
0.2	17.28	17.36	18.36	18.32	12.16	12.79
0.5	11.45	11.65	12.30	12.57	11.29	11.76
1	7.959	8.134	9.206	9.467	10.85	11.15
2	5.153	5.239	7.337	7.318	10.44	10.62
5	2.511	2.540	5.467	5.496	9.931	9.963
10	1.315	1.334	4.619	4.586	9.587	9.505
20	0.658	0.660	3.989	3.939	9.272	9.123

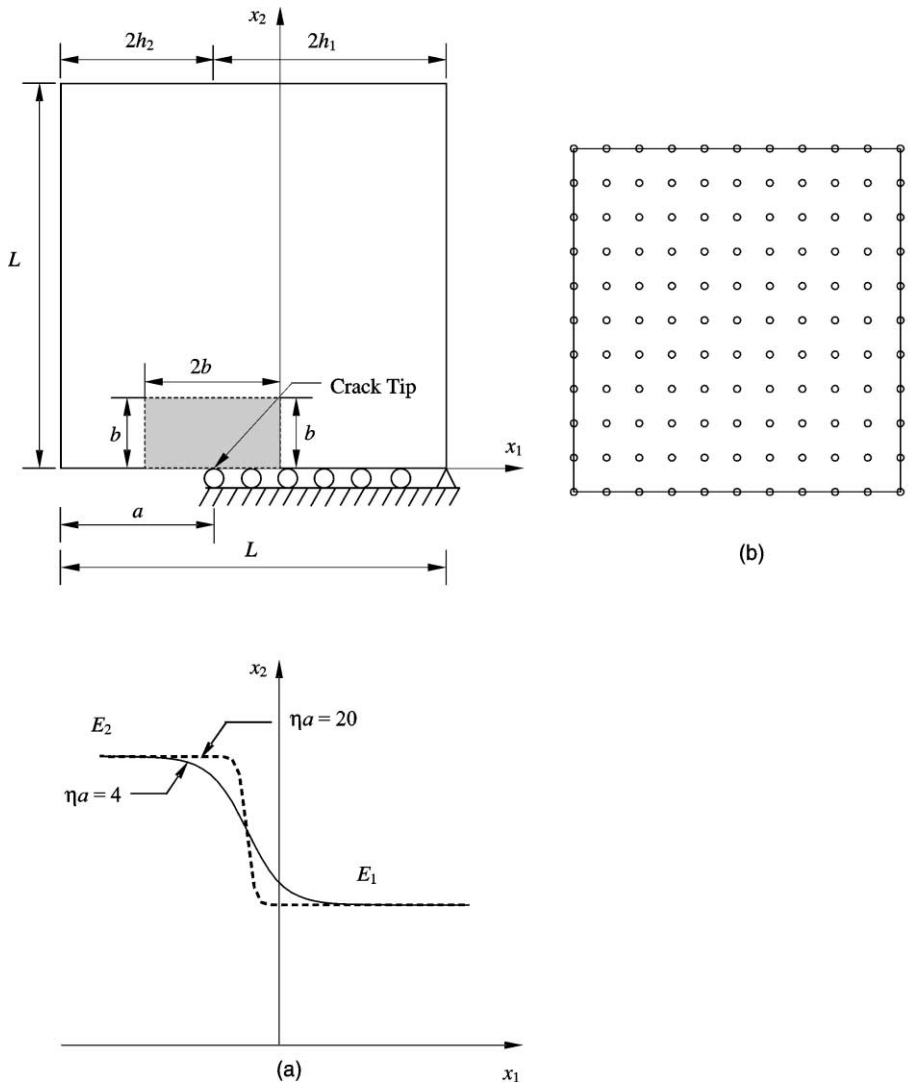

Fig. 4. Composite strip under mode-I loading: (a) geometry and elastic modulus variation; (b) meshless discretization (121 nodes).

$$E(x_1) = \frac{E_1 + E_2}{2} + \frac{E_1 - E_2}{2} \tanh[\eta(x_1 + 0.1)], \quad -0.5 \leqslant x_1 \leqslant 0.5, \tag{82}$$

where E_1 and E_2 are the bounds of $E(x_1)$, and η is a non-homogeneity parameter that controls the variation of $E(x_1)$ from E_1 to E_2, as shown in Fig. 4(a). When $\eta \to \infty$, a sharp discontinuity occurs in the slope of $E(x_1)$ across the interface at $x_1 = -0.1$. A tensile load corresponding to $\sigma_{22}(x_1, 1) = \bar{\varepsilon}E(x_1)/(1 - \nu^2)$ was applied at the top edge, which results in a uniform strain $\varepsilon_{22}(x_1, x_2) = \bar{\varepsilon}$ in the corresponding uncracked structure. The following numerical values were used: $E_1 = 1$ unit, $E_2 = 3$ units, $\eta a = 0$, 2, 4, 6, and 20 units, and $\bar{\varepsilon} = 1$. A plane strain condition was assumed.

A meshless discretization consisting of 121 uniformly distributed nodes is shown in Fig. 4(b). The domain of the plate was divided by 10×10 rectangular cells with their nodes coincident to the meshless nodes solely

Table 5
Normalized mode-I SIF for a composite strip configuration

ηa	$\frac{K_I}{\bar{\varepsilon}E(-0.5)\sqrt{\pi a}}$		
	Proposed method-I $[\widetilde{M}^{(1,2)}]$	Proposed method-II $[\widetilde{M}^{(1,2)}]$	Eischen [16]
0	2.133	2.133	2.112
2	2.304	2.348	2.295
4	2.589	2.670	2.571
6	2.769	2.879	2.733
20	3.314	3.579	3.228

Table 6
Domain independence of normalized mode-I SIF for a composite strip configuration

Method	Domain size ($2b \times b$)	$\frac{K_I}{\bar{\varepsilon}E(-0.5)\sqrt{\pi a}}$				
		$\eta a = 0$	$\eta a = 2$	$\eta a = 4$	$\eta a = 6$	$\eta a = 20$
Proposed method-I $[\widetilde{M}^{(1,2)}]$	0.15×0.075	2.108	2.276	2.547	2.716	3.252
	0.20×0.1	2.133	2.304	2.589	2.769	3.314
	0.25×0.125	2.145	2.324	2.620	2.807	3.354
Proposed method-II $[\widetilde{M}^{(1,2)}]$	0.15×0.075	2.108	2.310	2.613	2.809	3.478
	0.20×0.1	2.133	2.348	2.670	2.879	3.579
	0.25×0.125	2.145	2.377	2.715	2.935	3.655

for the purposes of numerical integration. The $\widetilde{M}^{(1,2)}$-integral was evaluated using both methods I and II over a domain size $2b \times b$ with $b = 0.1$ units, as shown in Fig. 4(a).

Table 5 compares the predicted normalized mode-I SIF $K_I/[\bar{\varepsilon}E(-0.5)\sqrt{\pi a}]$ obtained by the proposed meshless methods I and II to Eischen's FEM results [16] for several values of ηa. The EFGM results obtained using methods I and II agree very well with the FEM results. For EFGM, the domain independence of the $\widetilde{M}^{(1,2)}$-integral was verified by employing three different integral domains sizes: $b = 0.075$, 0.1, and 0.125 units. Table 6 shows the results of normalized SIF as a function of the integral domain size. The SIFs are accurate and stable regardless of the size of the integral domain and the type of the auxiliary field.

5.4. Example 4: slanted crack in a plate under mixed mode

Consider a slanted crack in a finite two-dimensional plate with length $L = 2$ units, width $W = 1$ unit and a 45° edge crack of normalized length $a/W = 0.4\sqrt{2}$, as shown in Fig. 5(a). The elastic modulus was assumed to follow an exponential function, given by

$$E(x_1) = \overline{E}\exp\left[\eta\left(x_1 - \frac{1}{2}\right)\right], \quad 0 \leqslant x_1 \leqslant W, \tag{83}$$

where $\overline{E}$ and η are two material parameters. For numerical values, $\overline{E} = 1$ unit and $\eta = 0$, 0.1, 0.25, 0.5, 0.75, and 1. The Poisson's ratio was held constant with $\nu = 0.3$. A plane stress condition was assumed. The applied load was prescribed along the upper edge with normal stress $\sigma_{22}(x_1, 1) = \bar{\varepsilon}\overline{E}\exp[\eta(x_1 - 0.5)]$, where $\bar{\varepsilon} = 1$. The displacement boundary condition was specified such that $u_2 = 0$ along the lower edge and, in addition, $u_1 = 0$ for the node at the right side of the lower edge.

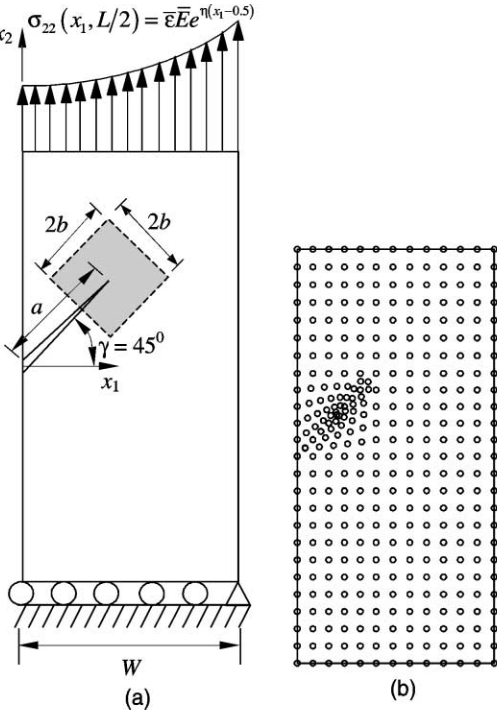

Fig. 5. Slanted crack in a plate under mixed-mode loading: (a) geometry and loads; (b) meshless discretization (370 nodes).

Table 7
Normalized SIFs for a slanted crack in a plate

η	Proposed method-I $[\widetilde{M}^{(1,2)}]$		Proposed method-II $[\widetilde{M}^{(1,2)}]$		Eischen [16]		Kim and Paulino [30] (J_k^*)	
	$\frac{K_I}{\bar{\varepsilon}\bar{E}\sqrt{\pi a}}$	$\frac{K_{II}}{\bar{\varepsilon}\bar{E}\sqrt{\pi a}}$	$\frac{K_I}{\bar{\varepsilon}\bar{E}\sqrt{\pi a}}$	$\frac{K_{II}}{\bar{\varepsilon}\bar{E}\sqrt{\pi a}}$	$\frac{K_I}{\bar{\varepsilon}\bar{E}\sqrt{\pi a}}$	$\frac{K_{II}}{\bar{\varepsilon}\bar{E}\sqrt{\pi a}}$	$\frac{K_I}{\bar{\varepsilon}\bar{E}\sqrt{\pi a}}$	$\frac{K_{II}}{\bar{\varepsilon}\bar{E}\sqrt{\pi a}}$
0	1.448	0.610	1.448	0.610	1.438	0.605	1.451	0.604
0.1	1.392	0.585	1.391	0.585	–[a]	–[a]	1.396	0.579
0.25	1.313	0.549	1.312	0.549	–[a]	–[a]	1.316	0.544
0.5	1.193	0.495	1.190	0.495	–[a]	–[a]	1.196	0.491
0.75	1.086	0.447	1.082	0.446	–[a]	–[a]	1.089	0.443
1	0.990	0.405	0.986	0.404	0.984	0.395	0.993	0.402

[a] Not available.

Fig. 5(b) shows a meshless discretization consisting of 370 nodes. The plate was divided into 336 cells for numerical integration. Both methods I and II were used to calculate the $\widetilde{M}^{(1,2)}$-integral with a domain size $2b \times 2b$ ($b = 0.045$ units), as shown in Fig. 5(a).

Table 7 provides a comparison of the predicted normalized SIFs $K_I/\bar{\varepsilon}\bar{E}\sqrt{\pi a}$ and $K_{II}/\bar{\varepsilon}\bar{E}\sqrt{\pi a}$, obtained by the proposed meshless methods I and II with Eischen's [16] and Kim and Paulino's [30] FEM results for several values of η. The agreement between the EFGM and FEM results is excellent. Using the EFGM method, the domain independence of SIF was verified by employing four different sizes of the integral domain parameter, e.g., $b = 0.045$, 0.05, 0.06, and 0.07 units. Table 8 shows the results of SIF for two extreme values of η ($\eta = 0$ and 1), as a function of the size of the integral domain. Very accurate and stable results of SIF were obtained regardless of the integral domain size and the type of the auxiliary field.

Table 8
Domain independence of normalized SIFs for a slanted crack in a plate

Method	Domain size ($2b \times b$)	$\eta = 0$		$\eta = 1$	
		$\frac{K_I}{\varepsilon\bar{E}\sqrt{\pi a}}$	$\frac{K_{II}}{\varepsilon\bar{E}\sqrt{\pi a}}$	$\frac{K_I}{\varepsilon\bar{E}\sqrt{\pi a}}$	$\frac{K_{II}}{\varepsilon\bar{E}\sqrt{\pi a}}$
Proposed method-I $[\widetilde{M}^{(1,2)}]$	0.09×0.09	1.448	0.610	0.990	0.405
	0.1×0.1	1.447	0.610	0.990	0.405
	0.12×0.12	1.447	0.610	0.990	0.405
	0.14×0.14	1.448	0.610	0.990	0.406
Proposed method-II $[\widetilde{M}^{(1,2)}]$	0.09×0.09	1.448	0.610	0.986	0.404
	0.1×0.1	1.447	0.610	0.984	0.403
	0.12×0.12	1.447	0.610	0.984	0.402
	0.14×0.14	1.449	0.610	0.984	0.403

5.5. Example 5: plate with an interior inclined crack under mixed mode

Consider a centrally located inclined crack of length $2a = 2$ units and an orientation γ in a finite two-dimensional square plate of size $2L = 2W = 20$ units, as shown in Fig. 6(a). Plane stress conditions were assumed with a constant Poisson's ratio of $\nu = 0.3$. The elastic modulus was assumed to be an exponential function, given by

$$E(x_1) = \overline{E}\exp(\eta x_1), \quad -W \leqslant x_1 \leqslant W, \tag{84}$$

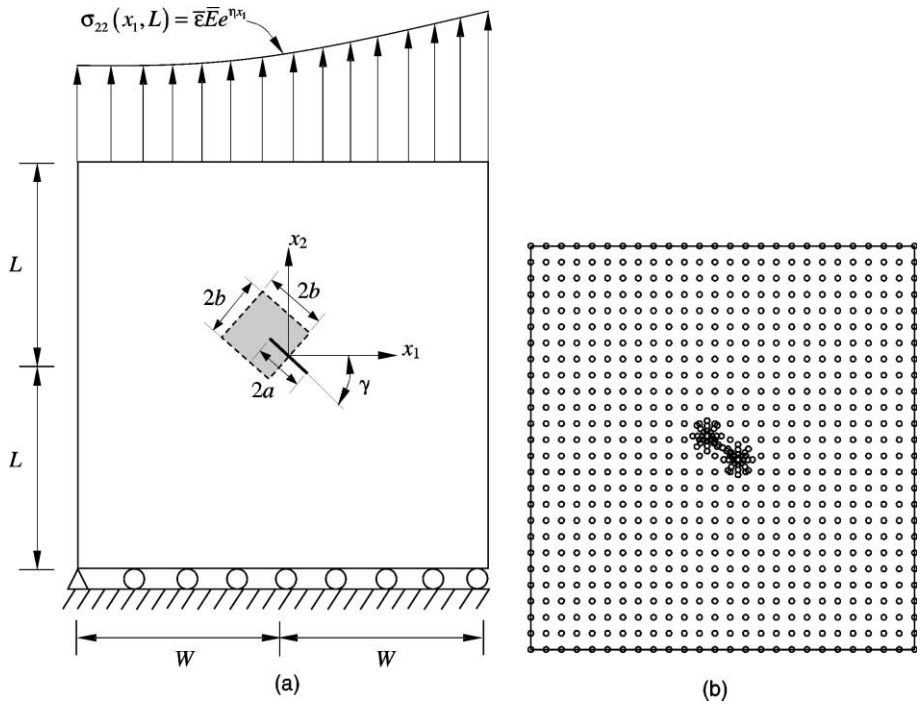

Fig. 6. Plate with an interior inclined crack under mixed-mode loading: (a) geometry and loads; (b) meshless discretization (740 nodes).

where $\overline{E}$ and η are material parameters. The following data were used for the numerical study: $\overline{E} = 1$ unit; $\eta = 0.25$ and 0.5; and $\gamma/\pi = 0$, 0.1, 0.2, 0.3, 0.4, and 0.5. The applied load corresponds to $\sigma_{22}(x_1, 10) = \bar{\varepsilon}\overline{E}\exp(\eta x_1)$, where $\bar{\varepsilon} = 1$. This stress distribution was obtained by applying nodal forces along the top edge of the plate. The displacement boundary condition was prescribed such that $u_2 = 0$ along the lower edge and, in addition, $u_1 = 0$ for the node at the left hand side of the lower edge. This loading results in a uniform strain $\varepsilon_{22}(x_1, x_2) = \bar{\varepsilon}$ in a corresponding uncracked structure.

The meshless discretization involves a total of 734 nodes for the cases in which $\gamma/\pi = 0$ and 0.5, and a total of 740 nodes for the cases in which $\gamma/\pi = 0.1$, 0.2, 0.3, and 0.4. The total number of nodes for the cases in which $\gamma/\pi = 0$ and 0.5 were divided as follows: 676 regularly distributed nodes, 10 additional nodes along the crack length, and 48 additional nodes in two crack tips (24 nodes in 3 rings around each crack tip). The total number of nodes for the cases in which $\gamma/\pi = 0.1$, 0.2, 0.3, and 0.4 were divided as follows: 676 regularly distributed nodes, 16 additional nodes along the crack length, and 48 additional nodes in the two crack tips (24 nodes in 3 rings around each crack tip). A typical nodal distribution for $\gamma/\pi = 0.2$ is shown in Fig. 6(b). The domain of the plate was divided by 25×25 rectangular cells with their nodes coincident to the regularly distributed 676 meshless nodes solely for the purposes of numerical integration. The inner radius of the coupling region for hybrid enrichment of the basis function was $0.5a$ and the outer radius was $0.75a$. Both methods I and II were used to evaluate the $\widetilde{M}^{(1,2)}$-integral with a domain size $2b \times 2b$ ($b = 0.3$ units), as shown in Fig. 6(a).

Konda and Erdogan [53] have investigated an infinite plate with such a configuration. Obviously, a meshless model cannot represent the infinite domains addressed in the analysis by Konda and Erdogan [53], but as long as the ratios a/W and a/L are kept relatively small (e.g., $a/W = a/L \leqslant 1/10$), the approximation is acceptable. Tables 9 and 10 provide a comparison between the predicted normalized SIFs $K_{\mathrm{I}}(a)/\overline{E}\bar{\varepsilon}\sqrt{\pi a}$ and $K_{\mathrm{I}}(-a)/\overline{E}\bar{\varepsilon}\sqrt{\pi a}$ for both crack tips, obtained by the proposed meshless methods I and II and those of Konda and Erdogan [53] for several values of γ/π, when $\eta = 0.25$ and $\eta = 0.5$, respectively. A reasonably good agreement is obtained between the EFGM results and Konda and Erdogan's [53] analytical solution.

Table 9
Normalized SIFs for a plate with an interior inclined crack ($\eta = 0.25$)

Method	γ/π	$\frac{K_{\mathrm{I}}(+a)}{\overline{E}\bar{\varepsilon}\sqrt{\pi a}}$	$\frac{K_{\mathrm{I}}(-a)}{\overline{E}\bar{\varepsilon}\sqrt{\pi a}}$	$\frac{K_{\mathrm{II}}(+a)}{\overline{E}\bar{\varepsilon}\sqrt{\pi a}}$	$\frac{K_{\mathrm{II}}(-a)}{\overline{E}\bar{\varepsilon}\sqrt{\pi a}}$
Proposed method-I [$\widetilde{M}^{(1,2)}$]	0	1.202	0.830	0	0
	0.1	1.176	0.801	−0.354	−0.263
	0.2	0.864	0.598	−0.572	−0.441
	0.3	0.424	0.293	−0.497	−0.421
	0.4	0.118	0.073	−0.307	−0.281
	0.5	0	0	0	0
Proposed method-II [$\widetilde{M}^{(1,2)}$]	0	1.194	0.813	0	0
	0.1	1.168	0.788	−0.349	−0.253
	0.2	0.858	0.590	−0.565	−0.426
	0.3	0.421	0.290	−0.494	−0.407
	0.4	0.117	0.072	−0.306	−0.276
	0.5	0	0	0	0
Konda and Erdogan [53]	0	1.196	0.825	0	0
	0.1	1.081	0.750	−0.321	−0.254
	0.2	0.781	0.548	−0.514	−0.422
	0.3	0.414	0.290	−0.504	−0.437
	0.4	0.121	0.075	−0.304	−0.282
	0.5	0	0	0	0

Table 10
Normalized SIFs for a plate with an interior inclined crack ($\eta = 0.5$)

Method	γ/π	$\frac{K_I(+a)}{\bar{E}\varepsilon\sqrt{\pi a}}$	$\frac{K_I(-a)}{\bar{E}\varepsilon\sqrt{\pi a}}$	$\frac{K_{II}(+a)}{\bar{E}\varepsilon\sqrt{\pi a}}$	$\frac{K_{II}(-a)}{\bar{E}\varepsilon\sqrt{\pi a}}$
Proposed method-I $[\widetilde{M}^{(1,2)}]$	0	1.418	0.665	0	0
	0.1	1.390	0.641	−0.381	−0.208
	0.2	1.016	0.488	−0.611	−0.361
	0.3	0.502	0.243	−0.517	−0.368
	0.4	0.145	0.057	−0.315	−0.262
	0.5	0	0	0	0
Proposed method-II $[\widetilde{M}^{(1,2)}]$	0	1.399	0.638	0	0
	0.1	1.370	0.620	−0.368	−0.192
	0.2	1.002	0.475	−0.596	−0.336
	0.3	0.496	0.238	−0.512	−0.345
	0.4	0.143	0.056	−0.313	−0.254
	0.5	0	0	0	0
Konda and Erdogan [53]	0	1.424	0.674	0	0
	0.1	1.285	0.617	−0.344	−0.213
	0.2	0.925	0.460	−0.548	−0.365
	0.3	0.490	0.247	−0.532	−0.397
	0.4	0.146	0.059	−0.314	−0.269
	0.5	0	0	0	0

Although all five examples presented in this paper are associated with a single crack, the proposed method is quite general and it should be applicable to fracture problems involving multiple cracks. However, a multiple-crack analysis at the current stage of method development will require a significantly larger effort and is outside the scope of the present study. Meshless analysis of multiple cracks in FGMs is a subject of current research by the authors.

6. Summary and conclusions

A Galerkin-based meshless method has been developed for calculating SIFs for a stationary crack in two-dimensional FGMs of arbitrary geometry. The method involves an EFGM, where the material properties are smooth functions of spatial coordinates and two newly developed interaction integrals for mixed-mode fracture analysis. The proposed interaction integral can also be implemented in conjunction with other numerical methods, such as the FEM. Five numerical examples, including both mode-I and mixed-mode problems, are presented to evaluate the accuracy of fracture parameters calculated by the proposed meshless method. Comparisons have been made between the SIFs predicted by the meshless method and available reference solutions in the literature, generated either analytically or numerically using various other fracture integrals or analyses. A good agreement is obtained between the results of the proposed meshless method and the previously obtained solutions.

Acknowledgements

The authors would like to acknowledge the financial support of the US National Science Foundation (NSF) under Award no. CMS-9900196. The NSF program director was Dr. Ken Chong. The authors would also like to thank Professor G. Paulino at the University of Illinois for his encouragement and guidance for working in the field of FGM.

References

[1] Suresh S, Mortensen A. Fundamentals of functionally graded materials. London: IOM Communications Ltd.; 1998.
[2] Hirano T, Teraki J, Yamada T. On the design of functionally gradient materials. In: Yamanouochi M, Koizumi M, Hirai T, Shiota I, editors. Proceedings of the First International Symposium on Functionally Gradient Materials, Sendai, Japan, 1990. p. 5–10.
[3] Igari T, Notomi A, Tsunoda H, Hida K, Kotoh T, Kunishima S. Material properties of functionally gradient material for fast breeder reactor. In: Yamanouochi M, Koizumi M, Hirai T, Shiota I, editors. Proceedings of the First International Symposium on Functionally Gradient Materials, Sendai, Japan, 1990. p. 209–14.
[4] Tani J, Liu GR. Surface waves in functionally gradient piezoelectric plates. JSME Int J Ser A (Mech Mater Eng) 1993;36(2):152–5.
[5] Osaka T, Matsubara H, Homma T, Mitamura S, Noda K. Microstructural study of electroless-plated CoNiReP/NiMoP double-layered media for perpendicular magnetic recording. Jpn J Appl Phys 1990;29(10):1939–43.
[6] Watanabe Y, Nakamura Y, Fukui Y, Nakanishi K. A magnetic-functionally graded material manufactured with deformation-induced martensitic transformation. J Mater Sci Lett 1993;12(5):326–8.
[7] Koike Y. Graded-index and single mode polymer optical fibers. In: Chiang LY, Garito AG, Sandman DJ, editors. Electrical, Optical, and Magnetic Properties of Organic Solid State Materials, Materials Research Proceedings, 247. Pittsburgh, PA: MRS; 1992. p. 817.
[8] Desplat JL. Recent developments on oxygenated thermionic energy converter—overview. Proceedings of the Fourth International Symposium on Functionally Graded Materials, Tsukuba City, Japan, 1996.
[9] Oonishi H, Noda T, Ito S, Kohda A, Yamamoto H, Tsuji E. Effect of hydroxyapatite coating on bone growth into porous titanium alloy implants under loaded conditions. J Appl Biomater 1994;5(1):23–7.
[10] Getto H, Ishihara S. Development of the fire retardant door with functionally gradient wood. Proceedings of the Fourth International Symposium on Functionally Graded Materials, Tsukuba City, Japan, 1996.
[11] Erdogan F. Fracture mechanics of functionally graded materials. Compos Eng 1995;5(7):753–70.
[12] Gibson RE. Some results concerning displacements and stresses in a nonhomogeneous elastic half space. Geotechnique 1967;17:58–67.
[13] Atkinson C, List RD. Steady state crack propagation into media with spatially varying elastic properties. Int J Eng Sci 1978;16:717–30.
[14] Dhaliwal RS, Singh BM. On the theory of elasticity of a nonhomogeneous medium. Int J Elasticity 1978;8:211–9.
[15] Delale F, Erdogan F. The crack problem for a nonhomogeneous plane. J Appl Mech 1983;50:609–14.
[16] Eischen JW. Fracture of nonhomogeneous materials. Int J Fract 1987;34:3–22.
[17] Jin ZH, Noda N. Crack tip singular fields in nonhomogeneous materials. J Appl Mech 1994;61:738–40.
[18] Jin ZH, Noda N. An internal crack parallel to the boundary of a nonhomogeneous half plane under thermal loading. Int J Eng Sci 1993;31:793–806.
[19] Erdogan F, Wu BH. Analysis of FGM specimens for fracture toughness testing. In: Proceedings of the Second International Symposium on Functionally Graded Materials, Ceramic Transactions, vol. 34. Westerville, Ohio: The American Ceramic Society; 1993. p. 39–46.
[20] Yang W, Shih CF. Fracture along an interlayer. Int J Solids Struct 1994;31:985–1002.
[21] Gu P, Asaro RJ. Cracks in functionally graded materials. Int J Solids Struct 1997;34:1–17.
[22] Gu P, Asaro RJ. Crack deflection in functionally graded materials. Int J Solids Struct 1997;34:3085–98.
[23] Tohgo K, Sakaguchi M, Ishii H. Applicability of fracture mechanics in strength evaluation of functionally graded materials. JSME Int J, Series-I 1996;39:479–88.
[24] Gu P, Dao M, Asaro RJ. A simplified method for calculating the crack tip field of functionally graded materials using the domain integral. J Appl Mech 1999;66:101–8.
[25] Anlas G, Santare MH, Lambros J. Numerical calculation of stress intensity factors in functionally graded materials. Int J Fract 2000;104:131–43.
[26] Marur PR, Tippur HV. Numerical analysis of crack tip fields in functionally graded materials with a crack normal to the elastic gradient. Int J Solids Struct 2000;37:5353–70.
[27] Bao G, Wang L. Multiple cracking in functionally graded ceramic/metal coatings. Int J Solids Struct 1995;32(19):2853–71.
[28] Bao G, Cai H. Delamination cracking in functionally graded coating/metal substrate systems. Acta Mech 1997;45(3):1055–66.
[29] Lee YD, Erdogan F. Residual/thermal stresses in FGM and laminated thermal barrier coatings. Int J Fract 1995;69:145–65.
[30] Kim JH, Paulino GH. Finite element evaluation of mixed mode stress intensity factors in functionally graded materials. Int J Numer Meth Eng 2002;53(8):1903–35.
[31] Zou ZZ, Wu SX, Li CY. On the multiple isoparametric finite element method and computation of stress intensity factor for cracks in FGMs. Key Eng Mater 2000;183–187:511–6.
[32] Rao BN, Rahman S. An efficient meshless method for fracture analysis of cracks. Comput Mech 2000;26:398–408.
[33] Belytschko T, Lu YY, Gu L. Crack propagation by element-free Galerkin methods. Eng Fract Mech 1995;51(2):295–315.

[34] Sukumar N, Moran B, Belytschko T. The natural element method in solid mechanics. Int J Numer Meth Eng 1998;43:839–87.
[35] Kaljevic I, Saigal S. An improved element free Galerkin formulation. Int J Numer Meth Eng 1997;40:2953–74.
[36] Belytschko T, Tabbara M. Dynamic fracture using element-free Galerkin methods. Int J Numer Meth Eng 1996;39:923–38.
[37] Fleming M, Chu YA, Moran B, Belytschko T, Lu YY, Gu L. Enriched element-free Galerkin methods for crack-tip fields. Int J Numer Meth Eng 1997;40:1483–504.
[38] Belytschko T, Krongauz Y, Organ D, Fleming M, Krysl P. Meshless methods: an overview and recent developments. Comp Meth Appl Mech Eng 1996;139:3–47.
[39] Anderson TL. Fracture mechanics—fundamentals and applications. 2nd ed. Boca Raton, FL: CRC Press; 1995.
[40] Yau JF, Wang SS, Corten HT. A mixed-mode crack analysis of isotropic solids using conservation laws of elasticity. J Appl Mech 1980;47:335–41.
[41] Shih CF, Asaro RJ. Elastic–plastic analysis of cracks on bimaterial interfaces. Part I. Small scale yielding. J Appl Mech 1988;55:299–316.
[42] Rice JR. A path independent integral and the approximate analysis of strain concentration by notches and cracks. J Appl Mech 1968;35:379–86.
[43] Moran B, Shih F. Crack tip and associated domain integrals from momentum and energy balance. Eng Fract Mech 1987;27:615–42.
[44] Honein T, Herrmann G. Conservation laws in homogeneous plane elastostatics. J Mech Phys Solids 1997;45(5):789–805.
[45] Dolbow J, Moës N, Belytschko T. Modeling fracture in Mindlin–Reissner plates with the extended finite element method. Int J Solids Struct 2000;37:7161–83.
[46] Gosz M, Dolbow J, Moran B. Domain integral formulation for stress intensity factor computation along curved three-dimensional interface cracks. Int J Solids Struct 1998;35(15):1763–83.
[47] Nahta R, Moran B. Domain integrals for axisymmetric interface crack problems. Int J Solids Struct 1993;30(15):2027–40.
[48] Dolbow JE, Gosz M. On the computation of mixed-mode stress intensity factors in functionally graded materials. Int J Solids Struct 2002;39(9):2557–74.
[49] Lancaster P, Salkauskas K. Surfaces generated by moving least squares methods. Math Comput 1981;37:141–58.
[50] Chen JS, Wang HP. New boundary condition treatments in mesh-free computation of contact problems. Comp Meth Appl Mech Eng 2000;187(3–4):441–68.
[51] Erdogan F, Wu BH. The surface crack problem for a plate with functionally graded properties. J Appl Mech 1997;64:449–56.
[52] Chen J, Wu L, Du S. Element free Galerkin methods for fracture of functionally graded materials. Key Eng Mater 2000;183–187:487–92.
[53] Konda N, Erdogan F. The mixed mode crack problem in a nonhomogeneous elastic medium. Eng Fract Mech 1994;47(4):533–45.